POLITECNICO DI TORINO
Repository ISTITUZIONALE

Updated shape monitoring of morphing wing structures using iFEM and SSB-iFEM: Applications to composite and modular architectures

Original
Updated shape monitoring of morphing wing structures using iFEM and SSB-iFEM: Applications to composite and modular architectures / Biscotti, V., Blaha, D., Ržika, M., Gherlone, M.. - In: AEROSPACE SCIENCE AND TECHNOLOGY. - ISSN 1270-9638. - ELETTRONICO. - 180:1(2027). [10.1016/j.ast.2026.113670]

Availability:
This version is available at: 11583/3015176 since: 2026-09-04T16:01:14Z

Publisher:
Elsevier

Published
DOI:10.1016/j.ast.2026.113670

Terms of use:

This article is made available under terms and conditions as specified in the corresponding bibliographic description in the repository

Publisher copyright

(Article begins on next page)

26 November 2026

Aerospace Science and Technology 180 (2027) 113670

Contents lists available at ScienceDirect

Aerospace Science and Technology

journal homepage: www.elsevier.com/locate/aescte

Original article

Updated shape monitoring of morphing wing structures using iFEM and SSB-iFEM: Applications to composite and modular architectures

Vincenzo Biscotti [a,*], David Blaha [b], Milan Růžička [b], Marco Gherlone [a]

[a] Politecnico di Torino, Department of Mechanical and Aerospace Engineering, Corso Duca degli Abruzzi 24, Torino, 10129, Italy
[b] Czech Technical University in Prague, Faculty of Mechanical Engineering, Technicka 4, Prague, 16000, Czech Republic

ARTICLE INFO

Communicated by Dr Kwok Kawai

Keywords:
Morphing wing
Modular wing architecture
Inverse finite element method (iFEM)
Single sensor based iFEM (SSB-iFEM)
Shape sensing
Levenberg-Marquardt control

ABSTRACT

Aircraft wings are traditionally designed as compromise configurations, able to provide acceptable performance over a range of flight conditions without being optimal at each operating point. Morphing-wing technologies, and trailing-edge morphing concepts in particular, can reduce this compromise by enabling continuous adaptation of the aerodynamic shape. In practical applications, however, achieving a prescribed morphing shape remains challenging, especially when aerodynamic loads reduce actuation authority and realistic sensor-placement constraints limit direct shape monitoring. This paper presents an updated iFEM-based closed-loop architecture for morphing-wing shape control and assesses it on two structures: a composite morphing trailing edge and a modular morphing wing. The first novelty is an updated control procedure based on the Levenberg-Marquardt algorithm, introduced to improve the stability and efficiency of the load-update process in the presence of aerodynamic disturbances, especially for flexible structures. The second novelty is the integration of Single Sensor Based inverse Finite Element Method (SSB-iFEM), which removes the need for fully back-to-back sensor layouts and enables shape sensing with single-sided or hybrid strain-sensor configurations. The third novelty is the extension of the framework from a single morphing trailing-edge device to a modular wing architecture with constrained sensor placement. Numerical results show that the updated procedure suppresses the oscillatory behavior exhibited by the original controller under severe aerodynamic loading while preserving convergence to the target shape. For the modular wing, the combined use of SSB-iFEM and a weighted load-update scheme enables shape control with limited sensor information, confirming the robustness and applicability of the proposed framework.

1. Introduction

Aircraft wings are traditionally designed as compromise configurations, able to ensure acceptable performance over a range of flight conditions, although not under fully optimal aerodynamic conditions at each operating point [1]. Morphing wing structures are intended to reduce this compromise by actively modifying selected geometric features of the wing, so that its aerodynamic shape can be better adapted to changing flight conditions and mission requirements [2]. In this way, morphing enables a closer-to-optimal aerodynamic behavior over an extended flight envelope, with potential benefits in terms of efficiency, control authority, and operational flexibility [3]. In recent years, morphing technologies have attracted increasing research interest in the aerospace community, mainly because of their potential contribution to more sustainable aviation through drag reduction, load control, and the consequent decrease in fuel consumption and emissions [4].

Among the various morphing-wing concepts proposed in the literature, trailing-edge morphing solutions have received particular attention because they enable a smoother and more continuous modification of the local airfoil camber than conventional hinged control surfaces [5]. This feature makes them especially attractive for improving the aerodynamic adaptation of the wing over changing operating conditions, and several studies have discussed their potential to enhance aerodynamic efficiency and overall wing performance in both maneuvering and high-lift conditions [6,7].

These promising aerodynamic capabilities have motivated a sustained research effort on morphing trailing-edge architectures within several research programs and technology demonstrators. From the DARPA/AFRL/NASA Smart Wing initiative [8], to European projects such as SARISTU [9], Clean Sky [10], MechaTwing [11], and HERWINGT [12], as well as industrially oriented developments such as the Mission Adaptive Compliant Wing by FlexSys [13], a considerable

* Corresponding author.
E-mail address: vincenzo.biscotti@polito.it (V. Biscotti).

https://doi.org/10.1016/j.ast.2026.113670
Received 10 May 2026; Received in revised form 28 July 2026; Accepted 26 August 2026
Available online 29 August 2026
1270-9638/© 2026 The Author(s). Published by Elsevier Masson SAS. This is an open access article under the CC BY license (http://creativecommons.org/licenses/by/4.0/).

effort has been devoted to the maturation of adaptive trailing-edge architectures. In parallel, a wide spectrum of technical solutions has been proposed, ranging from adaptive flaps [14] and compliant trailing-edge structures [15,16], to smart-actuation [17], multistable concepts [18], and bio-inspired mechanisms [19,20].

Despite the wide variety of architectures proposed in the literature, these solutions share a common objective: achieving target shape configurations that are best suited to the current aerodynamic condition, so as to maximize wing performance. In practical applications, however, attaining a prescribed morphing shape is far from trivial, since the structure must remain compliant enough to deform while being sufficiently stiff to withstand aerodynamic loads, which may significantly affect the available actuation authority under real operating conditions [21,22].

Several control strategies have therefore been proposed for morphing wing structures, relying on different feedback variables, sensing technologies, and control architectures [23,24]. In many cases, the control action is driven either by quantities only indirectly related to the actual wing shape or by measurements associated with local structural parameters. More recently, Biscotti et al. investigated a different perspective, placing particular emphasis on global shape reconstruction within the control-loop [25]. In their study, the feedback was provided by the inverse Finite Element Method (iFEM) [26], a shape-sensing technique that reconstructs the global deformed structural configuration and thus enables direct monitoring of the actual morphed shape.

Shape sensing refers to the reconstruction of the deformed configuration of a structure from discrete strain measurements, with the aim of obtaining global information on the displacement field for monitoring, diagnostics, and control purposes. Within this general framework, several families of methods have been proposed, including strain-integration approaches such as Ko's Displacement Theory, basis-function approaches such as the Modal Method, and finite-element-based variational approaches such as the inverse Finite Element Method (iFEM) [27]. Although the first two classes have proved effective in a number of applications, their performance may be affected by kinematic simplifications, by the need for prior modal information, or by reduced adaptability to complex structures and full-field monitoring tasks [27]. By contrast, iFEM reconstructs the global displacement field by minimizing the least-squares error between analytical strains, obtained from a finite element discretization, and experimentally measured ones, while relying only on strain-displacement relations and therefore requiring no a priori knowledge of material properties or applied loads [26].

Comparative investigations have shown that, when a sufficiently rich strain dataset is available, iFEM generally provides higher reconstruction accuracy than alternative shape-sensing methods, albeit at the cost of a significant number of strain measurements [27–29]. This practical limitation can be addressed through two complementary routes, namely by increasing the amount of physically measured strain information or by enriching the strain field virtually before the reconstruction step. On the physical side, fibre-optic technologies, including FBGs and distributed fibre-optic sensing, make it possible to acquire denser strain information than conventional point-wise layouts [30]. On the virtual side, strain pre-extrapolation strategies such as Smoothing Element Analysis and Modal Virtual Sensor Expansion can enrich the strain field before the iFEM reconstruction, thus reducing the number of physical sensors required [31,32]. Related studies have also explored the combination of iFEM with neural networks to infer missing strain information from limited measurements [33], as well as Fisher-information-based strategies for systematic sensor placement [34]. An additional step forward is represented by the Single Sensor Based iFEM [35], a novel iFEM formulation that removes the need for back-to-back sensor arrangements and extends the applicability of the method to thin-walled structures instrumented with single-sided configurations [35]. Recent results have also shown that this increased flexibility can be exploited to identify hybrid and optimized sensor layouts, thereby reducing the number of sensors required while preserving an accuracy comparable to that of standard iFEM [36].

These accuracy- and applicability-driven needs have contributed to the rapid evolution of iFEM. Since its introduction [26], the method has grown into a broad methodological framework, with numerous inverse elements, enhanced kinematic assumptions, nonlinear extensions, damage-oriented developments, and hybrid or data-enriched strategies proposed in the literature; a comprehensive overview of these advances is beyond the scope of the present work and can be found in the recent review of Khalid et al. [37]. Owing to these developments, iFEM has progressively evolved from a promising inverse formulation into a versatile monitoring tool, finding applications in real-time structural monitoring and digital-twin implementation [38,39], in damage detection and localization [40–42], and in broader data-fusion and population-based SHM frameworks [43]. At the same time, its applicability has been demonstrated over a wide range of structural domains, including aircraft and aerospace structures [44–48], marine and offshore structures [49–52], and civil infrastructure [53–56].

Despite this broad spectrum of applications, direct iFEM applications to morphing structures remain comparatively scarce in the open literature. One example, for instance, is the work of Huang et al., who have explored shape-sensing strategies for morphing-wing load-bearing structures, focusing on reducing the number of nodal DOFs and improving computational efficiency [57]. Against this background, the work of Biscotti et al. [25] is particularly relevant, as it not only addressed a morphing application, but also showed that an iFEM-based closed-loop strategy can successfully drive a morphing trailing edge toward prescribed target configurations even when aerodynamic loading is taken into account. At the same time, that study highlighted a limitation of the original load-update law, whose iterative response may exhibit pronounced oscillations and require a large number of iterations to reach convergence under severe loading conditions.

To address this drawback, the present work proposes an updated control architecture in which the actuation loads are computed through a Levenberg-Marquardt-based procedure [58,59]. The update strategy is introduced with the aim of improving the stability and efficiency of the closed-loop response while preserving the shape-sensing capabilities of the original iFEM-based framework, and its performance is demonstrated on the composite morphing trailing edge structure originally tested by Biscotti et al. [25]. Moreover, to assess the proposed control scheme on a more challenging benchmark, the study also considers a modular morphing wing architecture inspired by the wind-tunnel demonstrator developed within the MechaTwing project [11]. This second application extends the investigation from a single morphing trailing-edge structure to a multi-module configuration that is more representative of realistic morphing-wing layouts. In addition, physical constraints on sensor placement are taken into account, particularly the limitations that prevent a fully back-to-back sensor configuration. Accordingly, the original iFEM-based control scheme is updated to incorporate the newly developed SSB-iFEM [35].

The remainder of the paper is organized as follows. Section 2 summarizes the methodological framework, including the iFEM and SSB-iFEM formulations, the original closed-loop control strategy, and the proposed Levenberg-Marquardt update. Section 3 describes the two morphing wing models considered in the study, namely the composite morphing trailing edge and the modular morphing wing. Section 4 presents and discusses the numerical results, while the main conclusions are finally drawn in Section 5.

2. Methodology

This Section provides an overview of the methods employed to develop the iFEM-based control-loop architecture presented in this work, which represents an update to the original one developed by Biscotti et al. [25]. In the updated procedure, both the inverse Finite Element Method (iFEM, [26]) and its new formulation, the Single Sensor Based iFEM (SSB-iFEM, [35]), are employed. Thus, first, the two formulations are introduced. Subsequently, a brief summary of the original

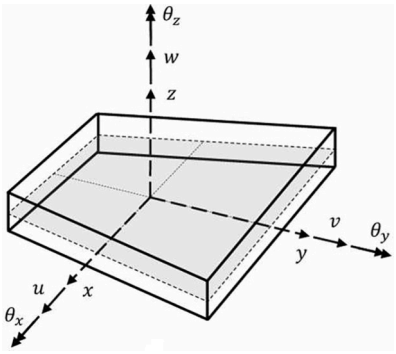

Fig. 1. Plate geometry and kinematic variables of the FSDT [46].

control scheme is provided. Lastly, the updated procedure, based on the Levenberg-Marquardt method [58,59], is described.

2.1. iFEM and SSB-iFEM formulations

This subsection briefly summarizes the original iFEM and its SSB formulation, which form the conceptual and numerical basis of the morphed shape control. Both approaches have been developed for thin plate and shell structures and are based on the kinematic assumptions of the First-order Shear Deformation Theory (FSDT) and on a corresponding finite element discretization. The key difference between iFEM and SSB-iFEM lies in the definition of the error functional, based on different analytical and experimental strain data.

2.1.1. Displacements, strains, and strain measures

A plate with thickness $2t$ is considered, with the thickness coordinate z ranging between $z = -t$ (bottom surface) and $z = +t$ (top surface). The reference plane is also the mid-surface and corresponds to the (x, y) plane, Fig. 1. According to FSDT, the displacement field of the plate is

$$\begin{aligned} u_x(x,y,z) &= u(x,y) + z\theta_y(x,y) \\ u_y(x,y,z) &= v(x,y) - z\theta_x(x,y) \\ u_z(x,y,z) &= w(x,y) \end{aligned} \tag{1}$$

where u_x, u_y, and u_z are the displacement components along the x, y, and z-axis, respectively. These components are expressed in terms of the kinematic variables, $\mathbf{u} = \{u, v, w, \theta_x, \theta_y\}^T$, namely the in-plane displacements of the mid-surface, u and v, the transverse deflection, w, and the bending rotations, θ_x and θ_y (refer to Fig. 1).

Within the small displacements and small strains regime, strain components are computed from Eq. (1) using linear relations

$$\begin{aligned} \boldsymbol{\varepsilon}_p &= \begin{Bmatrix} \varepsilon_{xx} \\ \varepsilon_{yy} \\ \gamma_{xy} \end{Bmatrix} = \begin{Bmatrix} u_{,x} \\ v_{,y} \\ u_{,y} + v_{,x} \end{Bmatrix} + z \begin{Bmatrix} \theta_{y,x} \\ -\theta_{x,y} \\ \theta_{y,y} - \theta_{x,x} \end{Bmatrix} \\ &= \mathbf{m}(\mathbf{u}) + z\mathbf{k}(\mathbf{u}) = \mathbf{Z}_{\varepsilon_p}(z) \begin{Bmatrix} \mathbf{m}(\mathbf{u}) \\ \mathbf{k}(\mathbf{u}) \end{Bmatrix} \end{aligned} \tag{2}$$

$$\boldsymbol{\gamma}_s = \begin{Bmatrix} \gamma_{xz} \\ \gamma_{yz} \end{Bmatrix} = \begin{Bmatrix} w_{,x} + \theta_y \\ w_{,y} - \theta_x \end{Bmatrix} = \mathbf{g}(\mathbf{u}) \tag{3}$$

with

$$\mathbf{Z}_{\varepsilon_p}(z) = \begin{bmatrix} \mathbf{I} & z\mathbf{I} \end{bmatrix} \tag{4}$$

The *in-plane strains* $\boldsymbol{\varepsilon}_p$ are expressed in terms of the *in-plane strain measures* $\mathbf{m}$ and $\mathbf{k}$ (membrane strains and bending curvatures, respectively), and the *transverse shear strains* $\boldsymbol{\gamma}_s$ correspond to the *transverse shear strain measures*, $\mathbf{g}$.

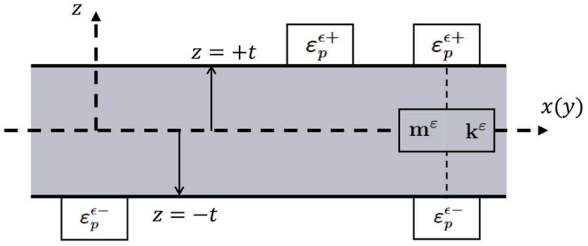

Fig. 2. Some discrete strain sensors on the top and bottom surfaces of a thin-walled structure. Experimental in-plane strain measures ($\mathbf{m}^\epsilon$ and $\mathbf{k}^\epsilon$) are available only where sensors are attached in a back-to-back configuration [39].

2.1.2. Finite element discretization

The plate structure is subdivided into finite elements and, for each element, the kinematic variables $\mathbf{u}$ are approximated using shape functions, $\mathbf{N}$, and nodal degrees of freedom (DOFs), $\mathbf{u}^e$,

$$\mathbf{u} = \mathbf{N}\mathbf{u}^e \tag{5}$$

Therefore, the strain field (Eqs. (2) and (3)) is approximated accordingly

$$\boldsymbol{\varepsilon}_p = \mathbf{m}(\mathbf{u}^e) + z\mathbf{k}(\mathbf{u}^e) = \mathbf{B}^m\mathbf{u}^e + z\mathbf{B}^k\mathbf{u}^e = \mathbf{Z}_{\varepsilon_p}(z) \begin{bmatrix} \mathbf{B}^m \\ \mathbf{B}^k \end{bmatrix} \mathbf{u}^e = \mathbf{Z}_{\varepsilon_p}(z)\mathbf{B}^{mk}\mathbf{u}^e \tag{6}$$

$$\boldsymbol{\gamma}_s = \mathbf{g}(\mathbf{u}^e) = \mathbf{B}^g\mathbf{u}^e \tag{7}$$

$\mathbf{B}^m$, $\mathbf{B}^k$, $\mathbf{B}^{mk}$ and $\mathbf{B}^g$ are matrices of shape-function derivatives obtained from $\mathbf{N}$. The inverse finite element adopted in the present paper is the quadrilateral, four-node iQS4, whose details (in particular its shape functions) can be found in Kefal et al. [60]. A key property of the iQS4 is the inclusion of the drilling rotation θ_z as one of the DOFs (Fig. 1). This inclusion leads to the availability of the full set of displacements and rotations as DOFs, and to the possibility to model curved and built-up structures.

2.1.3. Strain measurements and experimental strain measures

In a standard measurement pattern, some strain sensors are attached to the external surfaces of a thin-walled structure, at the top ($z = +t$) and/or at the bottom ($z = -t$), see Fig. 2. At each in-plane discrete location, these sensors provide the corresponding top and/or bottom *in-plane strain measurements*

$$\boldsymbol{\varepsilon}_p^{\epsilon+} = \begin{Bmatrix} \varepsilon_{xx}^{\epsilon+} \\ \varepsilon_{yy}^{\epsilon+} \\ \gamma_{xy}^{\epsilon+} \end{Bmatrix}, \qquad \boldsymbol{\varepsilon}_p^{\epsilon-} = \begin{Bmatrix} \varepsilon_{xx}^{\epsilon-} \\ \varepsilon_{yy}^{\epsilon-} \\ \gamma_{xy}^{\epsilon-} \end{Bmatrix} \tag{8}$$

where the superscript ϵ denotes the experimental origin of the quantity. When sensors are arranged in a back-to-back configuration (Fig. 2), the corresponding *experimental in-plane strain measures*, $\mathbf{m}^\epsilon$ and $\mathbf{k}^\epsilon$, can be evaluated as

$$\mathbf{m}^\epsilon = \frac{1}{2}(\boldsymbol{\varepsilon}_p^{\epsilon+} + \boldsymbol{\varepsilon}_p^{\epsilon-}), \qquad \mathbf{k}^\epsilon = \frac{1}{2t}(\boldsymbol{\varepsilon}_p^{\epsilon+} - \boldsymbol{\varepsilon}_p^{\epsilon-}) \tag{9}$$

Since transverse shear strains cannot be experimentally measured on thin-walled structures, the *experimental transverse shear strain measures*, $\mathbf{g}^\epsilon$, are always unavailable.

2.1.4. iFEM error functional

The iFEM functional for a single inverse element is the weighted sum of the least-squares errors between each analytical strain measure ($\mathbf{m}$, $\mathbf{k}$, $\mathbf{g}$) and the corresponding experimental strain measure ($\mathbf{m}^\epsilon$, $\mathbf{k}^\epsilon$, $\mathbf{g}^\epsilon$)

$$\Phi^e(\mathbf{u}^e) = \boldsymbol{\lambda}_m \cdot \boldsymbol{\Phi}_m(\mathbf{u}^e) + \boldsymbol{\lambda}_k \cdot \boldsymbol{\Phi}_k(\mathbf{u}^e) + \boldsymbol{\lambda}_g \cdot \boldsymbol{\Phi}_g(\mathbf{u}^e) \tag{10}$$

$\boldsymbol{\lambda}_m$, $\boldsymbol{\lambda}_k$, and $\boldsymbol{\lambda}_g$ are the vectors of penalty weights, and $\boldsymbol{\Phi}_m$, $\boldsymbol{\Phi}_k$, and $\boldsymbol{\Phi}_g$ are the vectors of individual errors corresponding to the membrane, curvature, and transverse shear strain measures, respectively,

$$\boldsymbol{\Phi}_m = \int_{A^e} \left[\mathbf{m}(\mathbf{u}^e) - \mathbf{m}^\epsilon\right]^{\circ 2} \mathrm{d}A^e \tag{11}$$

$$\boldsymbol{\Phi}_k = (2t)^2 \int_{A^e} \left[\mathbf{k}(\mathbf{u}^e) - \mathbf{k}^\epsilon\right]^{\circ 2} \mathrm{d}A^e \tag{12}$$

$$\boldsymbol{\Phi}_g = \int_{A^e} \left[\mathbf{g}(\mathbf{u}^e) - \mathbf{g}^\epsilon\right]^{\circ 2} \mathrm{d}A^e \tag{13}$$

where A^e is the area of the element and the operator $(\cdot)^{\circ 2}$ represents the Hadamard power.

The penalty weights $\boldsymbol{\lambda}_m$, $\boldsymbol{\lambda}_k$, and $\boldsymbol{\lambda}_g$ govern the level of compatibility enforcement between analytical and experimental strain measures. Furthermore, these coefficients allow to account for missing experimental strain data in an inverse element. Specifically, the penalty weight is assigned a value of unity when the corresponding experimental strain measure is accessible; conversely, in instances where an experimental strain measure is unavailable, a small value (e.g., 10^{-5}) is applied to minimize the influence of the missing data. Since transverse shear strain measures $\mathbf{g}^\epsilon$ cannot be measured experimentally, they are assumed to be $\mathbf{0}$; small values are assigned to the associated penalty weights, $\boldsymbol{\lambda}_g = \{10^{-5}, 10^{-5}\}$, and the corresponding least-squares error assumes a simplified definition

$$\boldsymbol{\Phi}_g = \int_{A^e} \mathbf{g}(\mathbf{u}^e)^{\circ 2} \mathrm{d}A^e \tag{14}$$

As for the experimental in-plane strain measures, $\mathbf{m}^\epsilon$ and $\mathbf{k}^\epsilon$, they require back-to-back sensors (Eq. (9)), thus leading to the condition $\boldsymbol{\lambda}_m = \boldsymbol{\lambda}_k$ and to the following cases: tri-axial strain rosettes $\boldsymbol{\lambda}_m = \boldsymbol{\lambda}_k = \{1, 1, 1\}$, no strain sensors at all $\boldsymbol{\lambda}_m = \boldsymbol{\lambda}_k = \{10^{-5}, 10^{-5}, 10^{-5}\}$, linear strain-gauges along the $y-$axis $\boldsymbol{\lambda}_m = \boldsymbol{\lambda}_k = \{10^{-5}, 1, 10^{-5}\}$ (and values modified accordingly if linear strain-gauges are measuring only ϵ_{xx} or γ_{xy}).

Substituting Eqs. (6) and (7) into Eqs. (11), (12) and (14), and these into the definition of the element error functional, Eq. (10), and then minimizing with respect to the element nodal DOFs, $\mathbf{u}^e$, yields the element-level system of linear algebraic equations

$$\frac{\partial \Phi^e(\mathbf{u}^e)}{\partial \mathbf{u}^e} = \mathbf{K}^e\mathbf{u}^e - \mathbf{f}^e = 0 \implies \mathbf{K}^e\mathbf{u}^e = \mathbf{f}^e \tag{15}$$

where the vector $\mathbf{u}^e$ collects the nodal DOFs of the inverse element; the coefficient matrix, $\mathbf{K}^e$, depends on the element shape functions and on the spatial distribution of the available strain measurements, whereas the right-hand-side vector, $\mathbf{f}^e$, additionally incorporates the corresponding experimental strain values (for the complete definition of the coefficient matrix, $\mathbf{K}^e$, and of the right-hand-side vector, $\mathbf{f}^e$, refer to Tessler et al. [26], or Biscotti et al. [35]). The transformation from local element coordinates to the global structural system, followed by the assembly of contributions from the whole set of inverse elements, yields the global algebraic system of equations

$$\mathbf{KU} = \mathbf{F} \tag{16}$$

where $\mathbf{U}$ represents the vector of nodal degrees of freedom (DOFs) for the discretized structure, while $\mathbf{K}$ and $\mathbf{F}$ are the corresponding global quantities obtained by assembling the element contributions. Accordingly, $\mathbf{K}$ is determined by the inverse finite element discretization and by the spatial distribution of the sensors, whereas $\mathbf{F}$ additionally depends on the corresponding experimental strain measurements. Thus, no information on either the applied loads or the material of the structure is required to compute its displacements. Furthermore, the computational efficiency of the solution (once appropriate geometric boundary conditions are imposed) is significantly enhanced by the fact that $\mathbf{K}$ does not change with the strain data. Consequently, even in dynamic analyses involving time-dependent variations of the strains and, thus, of $\mathbf{F}$, the inversion of $\mathbf{K}$ is required only once [26].

2.1.5. SSB-iFEM error functional

The SSB-iFEM error functional has a weighted-sum structure similar to that of iFEM (Eq. (10)), but is based on analytical strains and experimental strain measurements (rather than analytical and experimental strain measures), in order to circumvent the difficulty or even infeasibility of back-to-back sensor arrangements

$$\Psi^e(\mathbf{u}^e) = \boldsymbol{\lambda}_p^+ \cdot \boldsymbol{\Psi}_p^+(\mathbf{u}^e) + \boldsymbol{\lambda}_p^- \cdot \boldsymbol{\Psi}_p^-(\mathbf{u}^e) + \boldsymbol{\lambda}_g \cdot \boldsymbol{\Psi}_g(\mathbf{u}^e) \tag{17}$$

Similarly to iFEM, $\boldsymbol{\lambda}_p^+$, $\boldsymbol{\lambda}_p^-$, and $\boldsymbol{\lambda}_g$ are the vectors of penalty weights and $\boldsymbol{\Psi}_p^+$, $\boldsymbol{\Psi}_p^-$, and $\boldsymbol{\Psi}_g$ are the vectors of individual error functionals

$$\boldsymbol{\Psi}_p^+ = \int_{A^e} \left[\boldsymbol{\varepsilon}_p(+t, \mathbf{u}^e) - \boldsymbol{\varepsilon}_p^{\epsilon+}\right]^{\circ 2} \mathrm{d}A^e \tag{18}$$

$$\boldsymbol{\Psi}_p^- = \int_{A^e} \left[\boldsymbol{\varepsilon}_p(-t, \mathbf{u}^e) - \boldsymbol{\varepsilon}_p^{\epsilon-}\right]^{\circ 2} \mathrm{d}A^e \tag{19}$$

$$\boldsymbol{\Psi}_g = \int_{A^e} \boldsymbol{\gamma}_s(\mathbf{u}^e)^{\circ 2} \mathrm{d}A^e = \int_{A^e} \mathbf{g}(\mathbf{u}^e)^{\circ 2} \mathrm{d}A^e = \boldsymbol{\Phi}_g \tag{20}$$

In addition to playing a role similar to that already discussed for iFEM, the vectors $\boldsymbol{\lambda}_p^+$, $\boldsymbol{\lambda}_p^-$ are also associated with a range of sensor configurations that is wider for SSB-iFEM than for iFEM. Since a back-to-back sensor layout is not required, $\boldsymbol{\lambda}_p^+$ and $\boldsymbol{\lambda}_p^-$ do not need to coincide. For example, if a linear strain gauge in the $x-$direction is available on the top surface only, $\boldsymbol{\lambda}_p^- = \{10^{-5}, 10^{-5}, 10^{-5}\}$ and $\boldsymbol{\lambda}_p^+ = \{1, 10^{-5}, 10^{-5}\}$. Eq. (20) reveals that the individual error functional $\boldsymbol{\Psi}_g = \boldsymbol{\Phi}_g$ represents a common term between iFEM and SSB-iFEM; therefore the same penalization strategy holds for the definition of $\boldsymbol{\lambda}_g$.

By substituting Eqs. (6) and (7) into Eqs. (18)–(20), and subsequently into Eq. (17), the SSB-iFEM error functional can be rewritten in terms of the nodal DOFs, $\mathbf{u}^e$. Performing minimization with respect to $\mathbf{u}^e$, followed by the transformation from the element to the structural coordinate system and by the global assembly, yields systems of equations analogous to Eq. (15) (for the element) and Eq. (16) (for the structure), but involving a modified definition of the coefficient matrices and of the right-hand-side vectors (see [26] and [35] for additional details).

The new system of equations maintains all the properties of the iFEM one, that is, independence from structural loads and material properties, applicability to static and dynamic cases, and a low computational cost of the solution procedure. However, it is worth highlighting once more that the SSB-iFEM allows building such a system of equations on the basis of single-sided, back-to-back, or hybrid sets of sensor configurations, in turn enabling higher flexibility in the sensor pattern selection compared to the iFEM.

2.2. Original closed-loop control architecture

This subsection summarizes the original iFEM feedback-based closed-loop strategy adopted for morphing wing shape control, first presented by Biscotti et al. [25]. The strategy is implemented at a numerical level, employing a FE model of the structure to simulate the real morphing wing actuation and deformation. Under the assumption that the FE data on the displacement of the structure, and thus on its shape, are unknown to the controller (as the actual shape of the structure would be in a real application), the iFEM is employed to constantly reconstruct and monitor the shape of the structure from its strain measurements, enabling the controller to assess whether the target shape has been achieved and, to this end, compute the required actuation loads. The control-loop flowchart is reported in Fig. 3.

At the generic iteration (time instant t), it proceeds as follows:

1. The difference between the target shape, $\mathbf{P}_{tgt}$, and the iFEM reconstructed shape, $\mathbf{P}_{iFEM}(t)$, is evaluated. This mismatch is used to define the required displacements, $\mathbf{D}_{req}(t)$, as

$$\mathbf{D}_{req}(t) = \mathbf{P}_{tgt} - \mathbf{P}_{iFEM}(t). \tag{21}$$

as well as the convergence criterion of the iterative process (its explicit expression depends on the specific application and is provided subsequently).

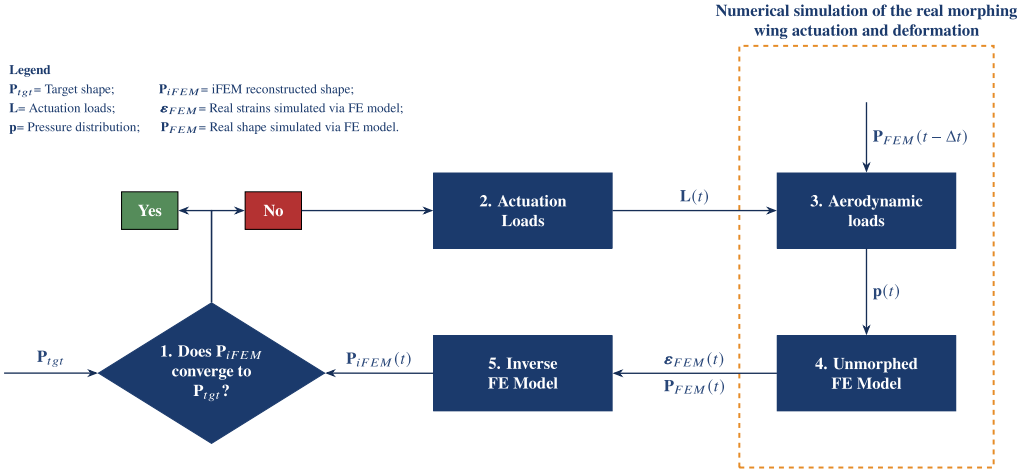

Fig. 3. Original closed-loop control architecture [25].

2. The computation of the actuation loads follows an influence-coefficients matrix approach, inspired by the work of Roy et al. [61]. For a given actuation scheme, the matrix of influence coefficients $\mathbf{C}$ relates each load increment to the corresponding displacement variation,

$$\mathbf{D}(t) = \mathbf{C}\,\Delta\mathbf{L}(t). \tag{22}$$

By enforcing $\mathbf{D}(t) = \mathbf{D}_{req}(t)$ in a least-squares sense, the load increment is computed as the solution to the problem

$$\min_{\Delta\mathbf{L}(t)} \left\| \mathbf{D}_{req}(t) - \mathbf{C}\Delta\mathbf{L}(t) \right\|^2 \tag{23}$$

which yields:

$$\Delta\mathbf{L}(t) = \left(\mathbf{C}^T\mathbf{C}\right)^{-1}\mathbf{C}^T\mathbf{D}_{req}(t), \tag{24}$$

Consequently, the actuation load vector is updated as follows

$$\mathbf{L}(t) = \mathbf{L}(t-\Delta t) + \Delta\mathbf{L}(t) \tag{25}$$

where $\mathbf{L}(t-\Delta t)$ represents the actuation load vector computed in the previous iteration.
3. The effect of external/environmental loads is introduced through a spanwise-constant aerodynamic pressure distribution, $\mathbf{p}(t)$, acting on the wing surfaces. As in the original application [25], in the ones considered in this work, $\mathbf{p}(t)$ is obtained from XFOIL [62], under the assumption of laminar flow distribution. The pressure distribution is computed by feeding XFOIL with the coordinates of the deformed mid-span cross-section of the wing. The shape data are extracted from $\mathbf{P}_{FEM}(t-\Delta t)$, the FEM simulation of the real shape, computed in the prior control iteration.
4. The actuation loads $\mathbf{L}(t)$ and the aerodynamic pressure distribution $\mathbf{p}(t)$ are applied to the direct FE model of the unmorphed structure, yielding the simulated wing deformation $\mathbf{P}_{FEM}(t)$ and the corresponding surface strains $\boldsymbol{\varepsilon}_{FEM}(t)$.
5. The FEM strains $\boldsymbol{\varepsilon}_{FEM}(t)$ are used as input to the iFEM analysis to reconstruct the current shape $\mathbf{P}_{iFEM}(t)$, which is then fed back to the controller, closing the loop.

2.3. Levenberg-Marquardt control

In the original control scheme, the load increment is computed from the influence-coefficients matrix, which yields a proportional-control behavior: at each iteration, the load increment is proportional to the required displacements (Eq. (24)), that is, to the mismatch between the iFEM-reconstructed shape and the target shape. To mitigate the convergence and robustness issues that may arise with a purely proportional update law, a new control-loop architecture based on the Levenberg-Marquardt algorithm (LM, [58,59]) is introduced (Fig. 4).

This approach improves the robustness of the iterative process by minimizing a cost function, J_t, which, at every iteration (time instant t), is defined as the squared L2-norm:

$$J_t = \left\| \mathbf{P}_{tgt} - \mathbf{P}_{iFEM}(t) \right\|^2 = \left\| \mathbf{D}_{req}(t) \right\|^2 \tag{26}$$

Using the influence matrix $\mathbf{C}$ defined in the previous section, the iterative update for the actuation loads is calculated as:

$$\Delta\mathbf{L}(t) = (\mathbf{A} + \lambda\boldsymbol{\Gamma})^{-1}\mathbf{C}^T\mathbf{D}_{req}(t) \tag{27}$$

where $\mathbf{A} = \mathbf{C}^T\mathbf{C}$, and λ and $\boldsymbol{\Gamma} = diag(\mathbf{A})$ are, respectively, the damping parameter and the matrix that characterize the LM method [58,59]. Both $\mathbf{A}$ and $\boldsymbol{\Gamma}$ are precomputed to optimize the control-loop efficiency. The damping parameter is initialized at $\lambda = \lambda_0$, and is adaptively scaled by a factor, based on the evolution of the cost function J_t. If J_t decreases, λ is divided by a down-scaling factor, λ_{df}. In the limit where $\lambda \to 0$, the update step simplifies to the least-squares solution of the original control scheme, Eq. (24), which provides quadratic convergence near the local minimum. Conversely, when the cost function increases, λ is multiplied by an up-scaling factor, λ_{uf}, to shift toward a gradient descent behavior. In the limit where $\lambda \to \infty$, the step direction aligns with the steepest descent:

$$\Delta\mathbf{L}(t) \approx \frac{1}{\lambda}\boldsymbol{\Gamma}^{-1}\mathbf{C}^T\mathbf{D}_{req}(t) \tag{28}$$

From a control perspective, the adaptive damping parameter λ is the main component governing the robustness of the LM update. When the cost function does not decrease, the increase in λ regularizes the matrix $\mathbf{A} = \mathbf{C}^T\mathbf{C}$ and reduces the magnitude of the subsequent load increment. Since each column of the influence-coefficients matrix $\mathbf{C}$ describes the displacement variation produced by a unit increment of the corresponding actuation load, the diagonal terms of $\boldsymbol{\Gamma} = diag(\mathbf{C}^T\mathbf{C})$ quantify the magnitude of these individual effects. The matrix $\boldsymbol{\Gamma}$ therefore weights the regularization of each load component in proportion to its predicted influence on the monitored displacements, rather than applying the same absolute damping to all components. In this sense, λ acts as an adaptive damping term in the load-update space: it promotes more conservative corrections after an unsuccessful iteration, whereas its reduction following a decrease in J_t progressively restores the faster least-squares behavior of the original scheme.

3. Morphing wing models

In addition to the updated control procedure, a new modular morphing wing model is tested in this work. This Section provides a detailed

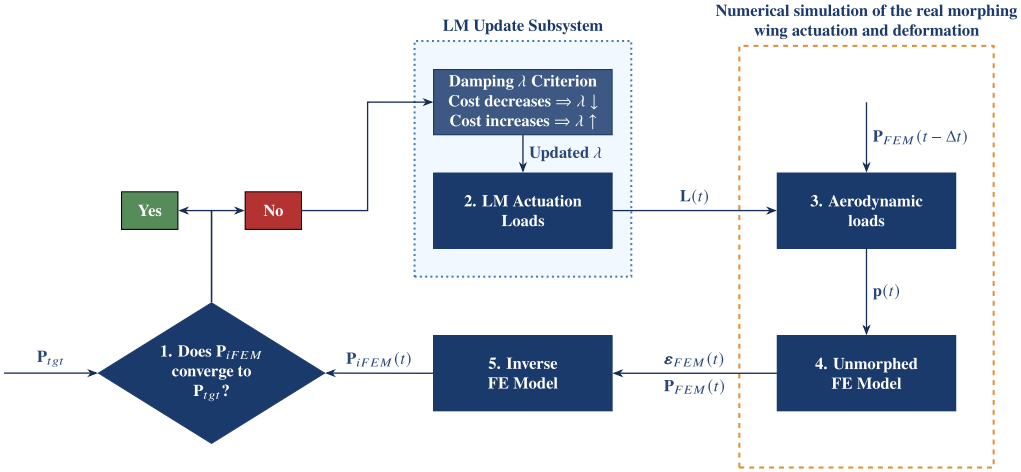

Fig. 4. New closed-loop control architecture with Levenberg-Marquardt update subsystem.

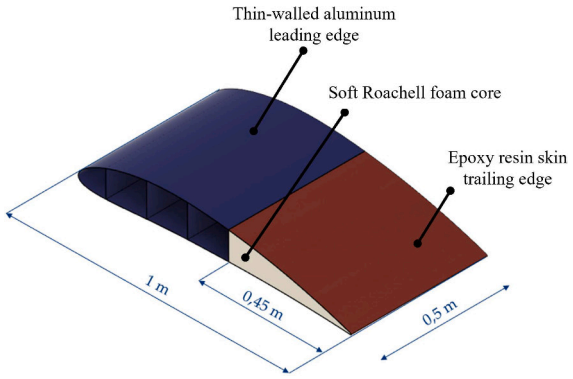

Fig. 5. Composite morphing trailing edge [25].

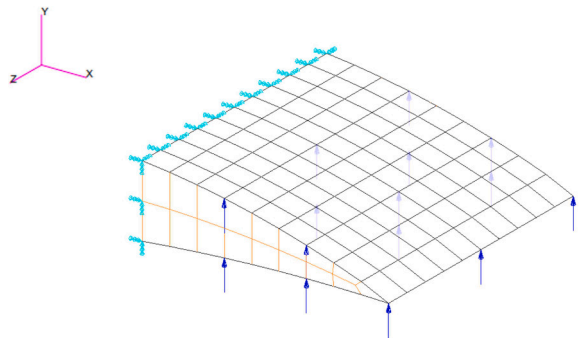

Fig. 6. Trailing-edge FE model and sparse transverse concentrated-forces actuation scheme [25].

description of the new morphing architecture. Additionally, as the new control procedure is also tested on the composite morphing trailing edge originally tested in [25], a brief summary of the original model is also included.

3.1. Composite morphing trailing edge

This subsection briefly recalls the composite morphing trailing-edge benchmark introduced in Biscotti et al. [25], which is retained unchanged to isolate the effects of the updated control strategy. The morphing capability is confined to the trailing edge and is employed to modify its camber. The reference 3D configuration is shown in Fig. 5.

The wing section is based on a NACA 6516 profile. The leading-edge portion, made of aluminum, thin-walled structures, is treated as infinitely rigid with respect to the compliant trailing edge. The latter consists of an epoxy-resin skin supported by a soft foam core. Material properties and thickness data are reported in [25].

3.1.1. Numerical models

The direct and inverse models adopted within the closed-loop procedure are presented in Fig. 6. Only the trailing-edge portion is modeled, while the interface with the rigid leading edge is represented through clamped boundary conditions applied at the front end of the trailing edge.

The direct FE model is developed in MSC/PATRAN and MSC/NASTRAN. The skin is discretized using QUAD4 shell elements and the core is modeled using HEX8 solid elements. In the present work, the trailing edge is actuated through a set of sparse transverse concentrated forces, acting along the global Y direction and distributed along both chord-wise and span-wise directions (Fig. 6). This actuation scheme is retained from [25] as a simplified representation of the structural action that may be transmitted by a real internal actuation mechanism [63,64]. It is intended to assess the closed-loop control strategy rather than to reproduce or size a specific actuator architecture; the physical interpretation and limitations of this idealization were discussed in the original study.

The iFEM discretization involves only the skin and adopts iQS4 inverse quadrilateral elements [60]. The iFEM mesh coincides with the 2D FEM mesh of the skin (Fig. 6), thus enabling a direct transfer of strain data from the FEM simulation to the iFEM reconstruction. In particular, it is assumed that a fully back-to-back configuration of strain rosettes, placed at the centroid of each of the elements of the iFEM mesh, is available. Consequently, all the in-plane, tri-axial strains on the top and bottom surfaces at the skin-element centroids are taken as known, consistently with [25].

3.1.2. Target shape and convergence metric

The target configuration is prescribed by modifying the camber line through a parabolic profile,

$$Y_{c,tgt}(X) = Y_{c0} - k\,(X - X_m)^2, \tag{29}$$

where Y_{c0} enforces continuity with the unmorphed portion of the wing and $X_m = 0.55$ defines the front boundary of the morphing trailing edge. In this work, as in [25], the target shape is generated using $k = 0.4$ (Fig. 7).

The effect of the weighting strategy becomes evident when the final iFEM reconstructions of Fig. 20 are compared with the corresponding unweighted noisy cases.

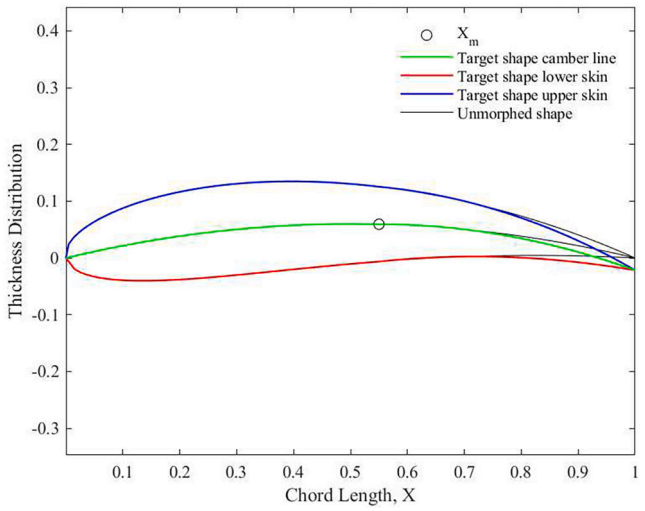

Fig. 7. Target shape for the composite morphing trailing edge ($k = 0.4$) [25].

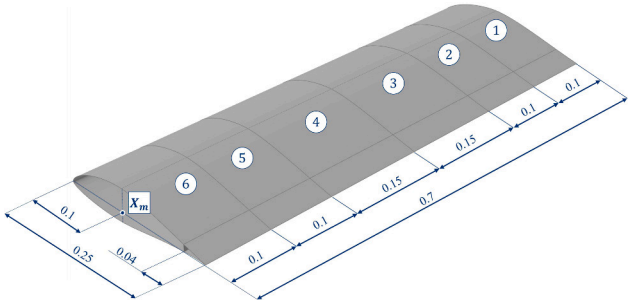

Fig. 8. Modular morphing wing architecture (dimensions are expressed in meters).

Since the deformation associated with camber morphing is predominantly transverse (global Y direction), convergence is monitored through a transverse relative least-squares metric. To compare the iFEM reconstructed shape with the target shape on a consistent set of coordinates, the target shape is mapped onto the chord-wise coordinates of the iFEM reconstruction via spline interpolation:

$$\begin{aligned} &\mathbf{Y} = f(\mathbf{X}), \\ &f = spline(\mathbf{X}_{tgt}, \mathbf{Y}_{tgt}), \\ &\mathbf{Y}^*_{tgt} = f(\mathbf{X}_{iFEM}), \end{aligned} \tag{30}$$

where $(\mathbf{X}_{tgt}, \mathbf{Y}_{tgt})$ define the target shape and $\mathbf{X}_{iFEM}$ contains the chord-wise coordinates of the nodes of the iFEM reconstructed shape. By selecting the proper sets of skin nodes, the transverse relative least squares error is computed for both the upper and lower skin of the morphing trailing edge as

$$err_{\Delta Y}(t) = \sqrt{\frac{1}{N_n} \frac{\sum_{j=1}^{N_n} \left((Y^*_{tgt})^j - Y^j_{iFEM}(t) \right)^2}{\max\left(\left(\mathbf{Y}^*_{tgt} \right)^2 \right)}}. \tag{31}$$

where N_n represents the total number of nodes of the upper (or lower) skin and the superscript j is used to represent the jth node of the FE discretization (for instance, Y^j_{iFEM} is the transverse coordinate of the jth node of the iFEM reconstruction).

3.2. Modular morphing wing

This subsection presents the new morphing wing considered in this work. The new wing adopts a modular architecture and is shown in Fig. 8, where dimensions are also provided.

The structure consists of six span-wise modules: two central modules (3 and 4) with a width of 0.15 m, and two end modules on each side with a width of 0.10 m (1, 2, 5, and 6). All modules share the same airfoil profile, namely the FX66-S196-V1. The adoption of both the selected profile and the modular layout is consistent with the morphing prototypes and the wind-tunnel demonstrator investigated within the WP4 of the MechaTwing Project [11]. Each module comprises a rigid front structure connected to a morphing trailing-edge section. The transition point between the rigid and the morphing section, shown in Fig. 8 as X_m, is placed at 40% of the chord length. The morphing concept and the actuation system are identical for all modules and are derived from the design proposed by Ameduri et al. [15]. In particular, the morphing trailing edge employs variable-thickness upper and lower skins connected by a vertical web. The upper skin is fixed at the front interface with the rigid structure, whereas the lower skin is linked to the actuation mechanism and slides on dedicated guides. This choice maintains a smooth upper surface, mitigates instability risks on the lower skin, and simplifies integration and maintenance. Actuation is achieved through an electromechanical system based on a ball-screw, combined with a linear guide and a mechanical transmission.

3.2.1. Finite element model

The FE model of a representative module (module 1) is shown in Fig. 9.

The model includes only the morphing trailing-edge portion and is built using QUAD4 shell elements, with an average global edge length of approximately 0.02 m. The modeling choices adopted for this module are replicated for all modules, and, as a simplifying assumption, the modules are treated as structurally independent, i.e., no constraints are imposed at the interfaces between adjacent modules. This assumption is consistent with modular morphing trailing-edge concepts in which neighboring modules are connected through highly compliant intermodular elements, such as flexible elastomeric skins or passive stretchable sections, designed to preserve surface continuity while limiting the mechanical coupling between adjacent active modules [22,65,66]. Accordingly, the structural interactions transferred through the interfaces are expected to be limited and are neglected in the present module-level FE model.

Consistently with [15], the front region of the upper skin is modeled as clamped. For the lower skin, the front region is constrained only along the Y_2 and Z_2 directions of the local reference system shown in Fig. 9 at the front interface of the lower skin. The actuation system is reproduced by prescribing a local displacement along the X_2 direction of the same reference system, thus emulating the pulling action transmitted by the electromechanical mechanism.

Fig. 9 also highlights the thickness distribution of the morphing components: the front region of the skin (black) has a thickness of 2.84 mm, which reduces in the rear region (blue) to 2.12 mm, while the vertical web (yellow) has a thickness of 2.74 mm.

3.2.2. iFE model and sensor layout

For the modular wing, the inverse model is built consistently with the structural discretization introduced in Section 3.2.1. In particular, the iFEM mesh coincides with the module-level FEM mesh and employs iQS4 inverse shell elements.

Within WP4 of the MechaTwing Project, the available sensing technology is based on Fibre Bragg Gratings (FBGs). Thus, a set of hybrid sensor configurations adopting uniaxial strain measurements is examined through an optimization process. Because the adopted actuation mechanism forces the lower skin of the morphing trailing edge to slide inside the rigid front part of the wing, the optimizations are performed under the constraint that no sensor can be placed on the external surface of the wing's lower skin. Under this constraint, the optimization space comprises all possible combinations of sensor lines among 15 chord-wise locations for the smaller modules (10 back-to-back on the upper skin and 5 single-sided on the lower skin) and 18 chord-wise locations

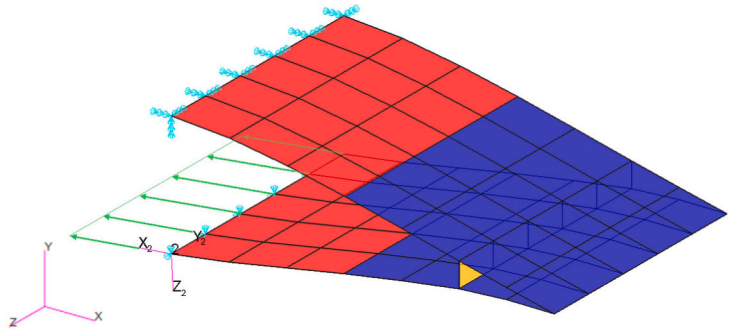

Fig. 9. Finite element model of a single morphing module (module 1).

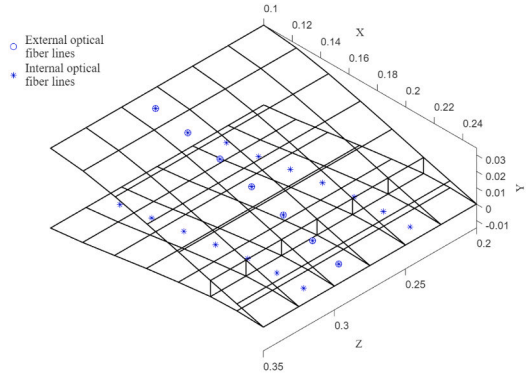

(a) Central modules (modules 3 and 4).

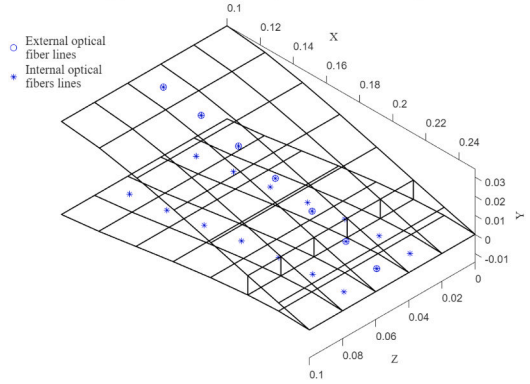

(b) Outer modules (modules 1, 2, 5, and 6).

Fig. 10. Optimized hybrid back-to-back and single-sided FBG sensor layout: four chord-wise fibre lines per module.

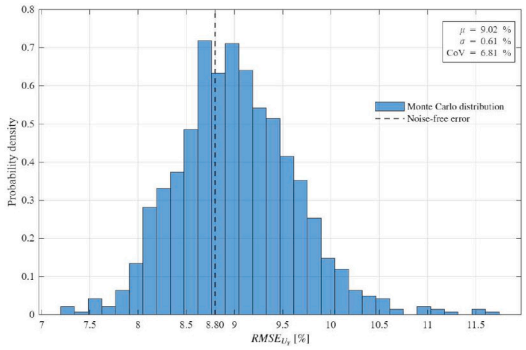

(a) Central-module layout (module 3).

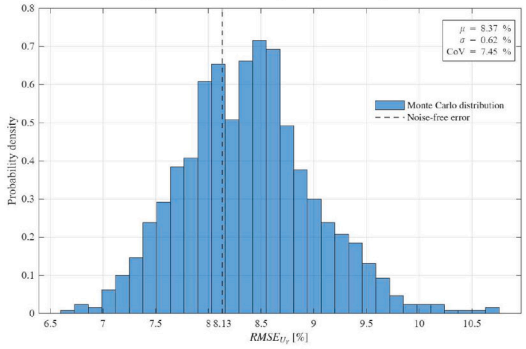

(b) Outer-module layout (module 1).

Fig. 11. Empirical probability-density functions of the global SSB-iFEM reconstruction error for a 10% strain-noise level.

for the larger modules (12 back-to-back on the upper skin and 6 single-sided on the lower skin). The resulting optimized sensor layout, obtained as a trade-off between the number of sensor lines and reconstruction accuracy, consists of four chord-wise FBG lines, two back-to-back on the upper skin and two single-sided on the inner surface of the lower skin. The optimized configurations are shown in Fig. 10: Fig. 10a refers to the central modules (3 and 4), while Fig. 10b refers to the outer ones (1, 2, 5 and 6). Since both back-to-back and single-sided strain data are available, shape reconstruction is performed via the Single Sensor Based formulation of iFEM (SSB-iFEM), previously introduced in Section 2.1.5.

The reconstruction performance of the optimized layouts is quantified through the global root-mean-square error of the transverse displacement component,

$$\mathrm{RMSE}_{U_Y} = 100\sqrt{\frac{1}{N_n}\frac{\sum_{j=1}^{N_n}\left(U^j_{Y,ref} - U^j_{Y,iFEM}\right)^2}{\max\left(\mathbf{U}_{\mathrm{Y,ref}}\right)^2}}, \tag{32}$$

where N_n is the number of nodes of the module, $U^j_{Y,ref}$ is the FEM transverse displacement at the jth node, and $U^j_{Y,iFEM}$ is the corresponding displacement reconstructed through iFEM or SSB-iFEM. The metric is evaluated for the unit actuation load used in the sensor-layout optimization.

To provide a direct comparison with conventional iFEM, the optimized hybrid layouts were converted into fully back-to-back configurations by adding two physical FBG lines per module on the external surface of the lower skin. This additional sensorization allows the membrane and bending strain measures required by standard iFEM to be evaluated at all four optimized chord-wise locations. However, it does not satisfy the installation constraint imposed by the sliding motion of the lower skin. As reported in Table 1, the fully back-to-back configu-

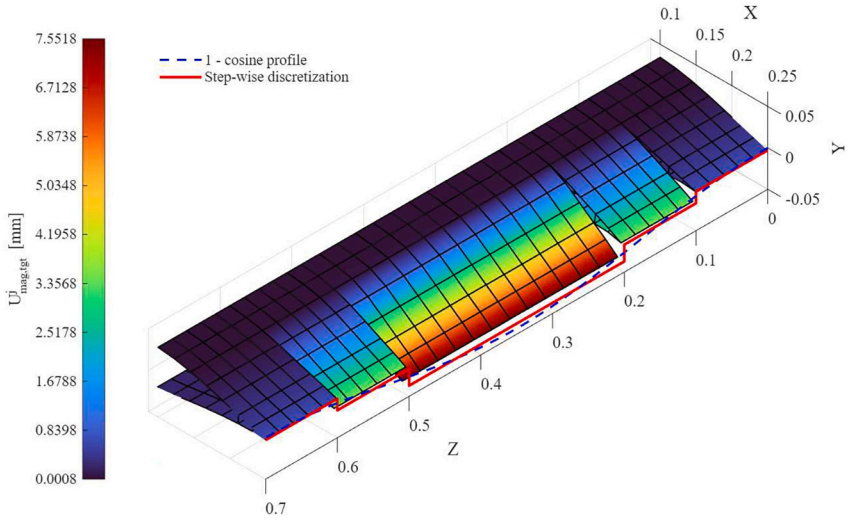

Fig. 12. One-cosine target shape (small deflection case); SF = 5; color-map: $U^j_{mag,tgt}$.

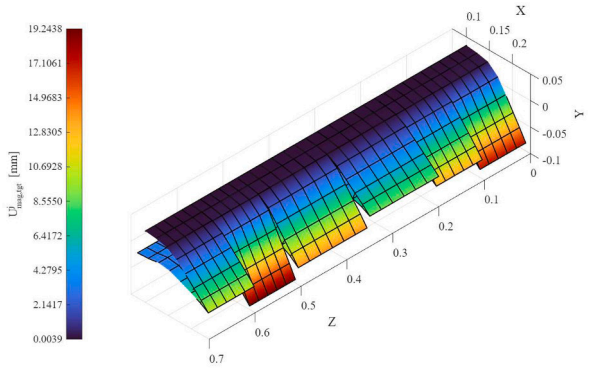

Fig. 13. Target shape for the large deflection case; SF = 5; color-map: $U^j_{mag,tgt}$.

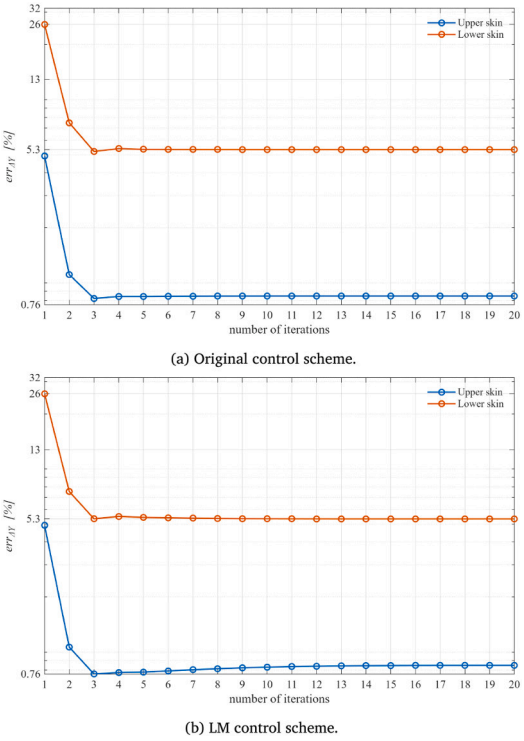

(a) Original control scheme.

(b) LM control scheme.

Fig. 14. Control scheme comparison, $V = 0$ m/s: history of $err_{\Delta Y}(t)$.

rations produce $RMSE_{U_Y}$ values of 2.23% for module 3 and 1.23% for module 1, compared with 8.80% and 8.13%, respectively, for the optimized hybrid SSB-iFEM layouts. Thus, the additional strain information provided by the fully back-to-back configuration improves the reconstruction accuracy, as expected. Nevertheless, the SSB-iFEM layout retains an error below 9% while requiring two fewer physical sensing lines per module and, most importantly, satisfying the actual installation constraints. The selected hybrid configuration therefore entails a moderate and practically acceptable loss of reconstruction accuracy in exchange for a physically feasible and less redundant sensor layout.

The robustness of iFEM-based shape reconstruction against measurement noise has previously been investigated for different structures, sensor arrangements, and uncertainty-propagation procedures [29,32,60]. To assess this aspect for the optimized layouts adopted here, an uncertainty-propagation analysis was performed using 1000 Latin Hypercube samples. An independent zero-mean Gaussian perturbation was applied to every active strain measurement, with a standard deviation equal to either 5% or 10% of the absolute nominal strain value. For the noisy cases, Table 1 reports the mean and standard deviation of $RMSE_{U_Y}$, together with its coefficient of variation.

The empirical probability-density distributions obtained for the more conservative 10% noise level are shown in Fig. 11.

The distributions remain concentrated around the corresponding noise-free values. In particular, the mean errors increase by less than 1% for all the modules, while the standard deviations remain equal to 0.6%. Measurement noise therefore mainly increases the dispersion of the reconstruction error, without introducing a substantial bias or altering the overall accuracy of the optimized shape-feedback layouts.

3.2.3. *Target shapes and convergence metric*

For the modular wing application, the procedure adopted for the composite trailing edge to define the target shapes (Section 3.1.2) cannot be applied directly, since analytical equations for the FX66-S196-V1 airfoil geometry are not available. In the context of the WP4 of the MechaTwing project, however, the morphing system is intended to replace a conventional hinged flap. Thus, the target shapes are defined so as to reproduce the geometry of a hinged-flap configuration.

Target airfoil coordinates are generated using XFOIL [62] by prescribing, for each module, a flap deflection angle β and setting the hinge location at 60% of the chord. Two target configurations are considered

Table 1
Shape-feedback reconstruction accuracy obtained with the optimized sensor layouts under noise-free and noisy strain inputs.

		Central modules (Module 3-4)		Outer modules (Module 1-2-5-6)	
Formulation and sensor layout	Noise level [%]	RMSE_{U_y} [%]	CoV [%]	RMSE_{U_y} [%]	CoV [%]
iFEM, fully back-to-back	0	2.23	–	1.23	–
SSB-iFEM, optimized hybrid	0	8.80	–	8.13	–
SSB-iFEM, optimized hybrid	5	8.85 ± 0.28	3.18	8.19 ± 0.29	3.51
SSB-iFEM, optimized hybrid	10	9.02 ± 0.61	6.81	8.37 ± 0.62	7.45

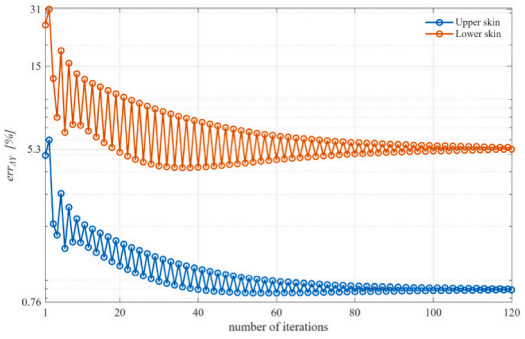

(a) Original control scheme.

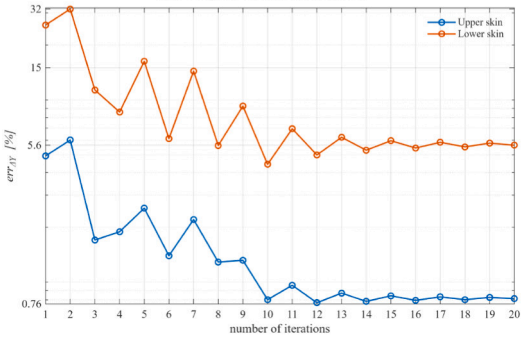

(b) LM control scheme.

Fig. 15. Control scheme comparison, $V = 300$ m/s: history of $err_{\Delta Y}(t)$.

in this work, namely a *small-deflection* and a *large-deflection* case. For the small-deflection target, moving along the positive Z-direction (i.e., from module 1 to 6 in Fig. 8), the following set of deflection angles is prescribed:

$$\boldsymbol{\beta} = [0.32, 1.93, 4.24, 4.24, 1.93, 0.32]^\circ \tag{33}$$

This sequence produces a step-wise discretization of a 1-cosine shape across the morphing modules, and it is shown in Fig. 12, where a scale factor (SF) of 5 is employed to magnify the morphing trailing edge deflections.

The large-deflection target, on the other hand, is defined by the following random set of flap deflection angles:

$$\boldsymbol{\beta} = [10, 7.5, 5, 8, 11, 6]^\circ \tag{34}$$

which yields the configuration reported in Fig. 13, where, as for the previous target shape, a scale factor of 5 is applied to better visualize the morphed target shape.

Both target shapes of Figs. 12 and 13 are also colored to display the target displacement values, that is, the displacement values required to achieve the target shape starting from the unmorphed configuration. In particular, for the jth node of the FE discretization, the color-maps show the displacement magnitude in the XY plane, computed as

$$U^j_{mag,tgt} = \sqrt{\left(U^j_{X,tgt}\right)^2 + \left(U^j_{Y,tgt}\right)^2} \tag{35}$$

Once the target profiles have been defined, convergence is assessed at module-level by measuring the distance between a set of points on the current module shape and the corresponding target airfoil contour. The procedure is outlined below for a representative module and is then applied independently to each module of the wing.

Let $(\mathbf{X}_{tgt}, \mathbf{Y}_{tgt})$ denote the discrete points describing the target airfoil curve of the module under consideration, generated through XFOIL [62], as explained in the previous subsection, and let $(\mathbf{X}_{iFEM}, \mathbf{Y}_{iFEM})$ denote the points of the module's current shape, reconstructed via the iFEM at a given iteration. Unlike the composite trailing-edge case (Section 3.1.2), analytical equations for the target airfoil geometry are not available in the present application. Therefore, the target airfoil contour is represented as a continuous parametric curve obtained from the discrete target points by introducing a normalized cumulative arc-length parametrization and fitting two cubic splines, one for the X coordinate and one for the Y coordinate. To this end, the target points are first ordered along the contour and associated with the normalized cumulative arc-length parameters

$$s^i_{tgt} = \frac{1}{S}\sum_{k=1}^{i-1}\sqrt{\left(X^{k+1}_{tgt} - X^k_{tgt}\right)^2 + \left(Y^{k+1}_{tgt} - Y^k_{tgt}\right)^2}, \qquad i = 1, \dots, M, \tag{36}$$

where the total arc length, S, is given by

$$S = \sum_{k=1}^{M-1}\sqrt{\left(X^{k+1}_{tgt} - X^k_{tgt}\right)^2 + \left(Y^{k+1}_{tgt} - Y^k_{tgt}\right)^2}. \tag{37}$$

and the superscripts i and k denote the points of the XFOIL discretization of the target airfoil (so as to distinguish them from the superscript j adopted for the FE discretization), and M is the total number of target airfoil points.

In analogy with the procedure adopted for the composite trailing edge, the spline interpolation of the target profile is written as

$$\begin{aligned} &X = f_X(s), \qquad Y = f_Y(s), \\ &f_X = spline(\mathbf{s}_{tgt}, \mathbf{X}_{tgt}), \qquad f_Y = spline(\mathbf{s}_{tgt}, \mathbf{Y}_{tgt}), \\ &X^*_{tgt}(\tau) = f_X(\tau), \qquad Y^*_{tgt}(\tau) = f_Y(\tau), \end{aligned} \tag{38}$$

with $\tau \in [0, 1]$ being the continuous curve parameter used to evaluate the spline-interpolated X and Y coordinates, X^*_{tgt} and Y^*_{tgt}.

This evaluation is instrumental as, for each point (X^j_{iFEM}, Y^j_{iFEM}) of the current reconstructed shape, it allows to assess and compute the minimum distance to the target curve $\left(X^*_{tgt}(\tau), Y^*_{tgt}(\tau)\right)$ as a solution of the following problem:

$$d_j = \min_{\tau\in[0,1]}\sqrt{\left(X^*_{tgt}(\tau) - X^j_{iFEM}\right)^2 + \left(Y^*_{tgt}(\tau) - Y^j_{iFEM}\right)^2} \tag{39}$$

In practice, the minimization in Eq. (39) is approximated by sampling the interpolated curve on a sufficiently dense set of τ values and selecting the minimum Euclidean distance, d_j.

Once the complete set of minimum-distance values between the target curve and each of the iFEM nodes has been obtained, the module-level convergence indicator at iteration t is finally computed through the following expression

$$err^m_d(t) = \sqrt{\frac{1}{N^m_n}\sum_{j=1}^{N^m_n} d_j^2}, \tag{40}$$

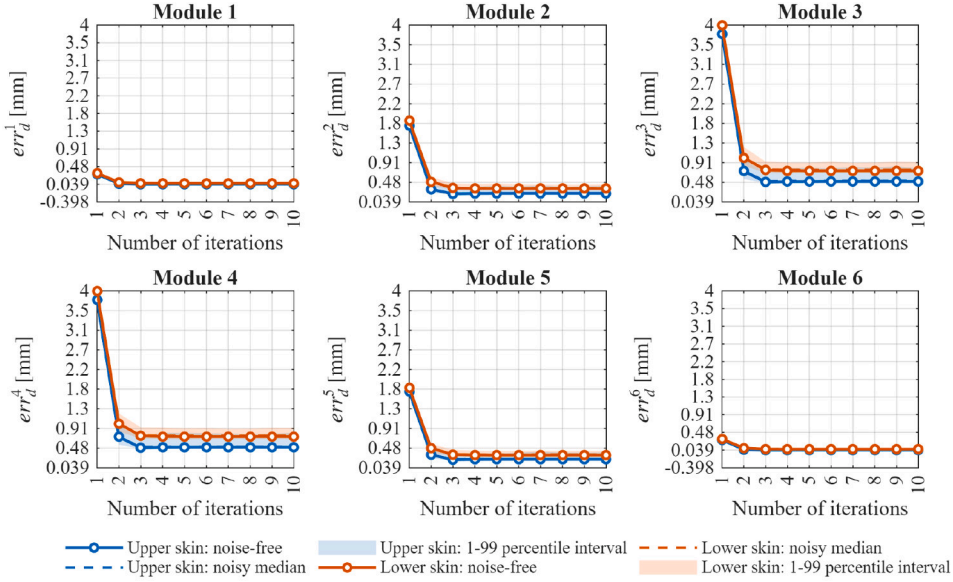

(a) 1-cosine target shape.

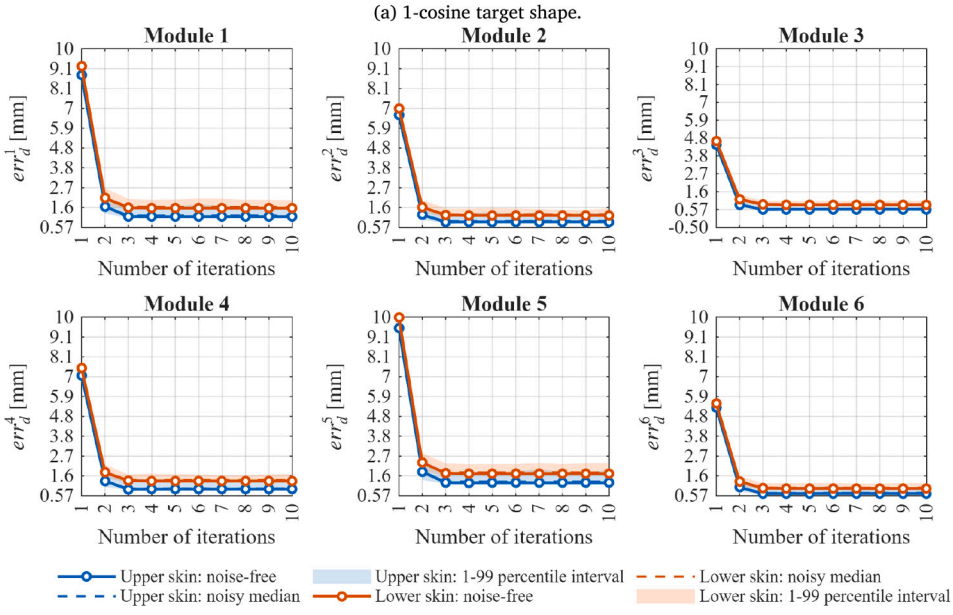

(b) Large-deflection target shape.

Fig. 16. Original control scheme, $V = 0$ m/s: noise-free and noisy histories of $err_d^m(t)$.

where the superscript m is used to refer to the mth module, and N_n^m is the number of iFEM nodes considered for the module. The root-mean-square error metric defined by Eq. (40) represents the average distance between the target shape and the iFEM-reconstructed shape, and it is measured in mm. Convergence of the modular wing is achieved when $err_d^m(t)$ falls below a prescribed threshold for each module.

4. Results

4.1. Composite morphing trailing edge

This subsection presents a numerical comparison between the original control strategy and the new LM-based one for the composite morphing trailing-edge structure. For the LM control scheme, the damping parameter is initially set to $\lambda_0 = 1 \times 10^{-3}$, while the down-scaling and up-scaling factors are chosen as $\lambda_{df} = 1.2$ and $\lambda_{uf} = 10$, respectively. To evaluate the performance of the updated control-loop architecture, a target shape defined by k = 0.4 is employed. The numerical assessment is conducted, as anticipated in Section 2.2, by introducing the aerodynamic pressure distribution, $\mathbf{p}$, as an external unknown load on the structure. A parametric analysis is performed, representing the pressure distribution as a function of the relative airstream velocity, V, as

$$\mathbf{p} = \frac{1}{2}\rho V^2 \mathbf{c_p} \tag{41}$$

where $\rho = 1.225\ kg/m^3$ is the air density and $\mathbf{c_p}$ is the vector of pressure coefficients obtained from XFOIL.

Fig. 14 illustrates the convergence behavior for the static case ($V = 0\ m/s$). In the absence of aerodynamic loads, both the original control scheme (Fig. 14a) and the LM-based architecture (Fig. 14b) rapidly converge to the target shape, with the latter requiring just a few additional iterations. Moreover, both approaches achieve the same final error, approximately 1% for the upper skin and 5% for the lower skin.

The advantages of the LM implementation become evident under high aerodynamic loading. The case where $V = 300$ m/s is therefore selected for the analysis. It should be noted that this case falls outside the optimal high-fidelity range of XFOIL and is not intended to repre-

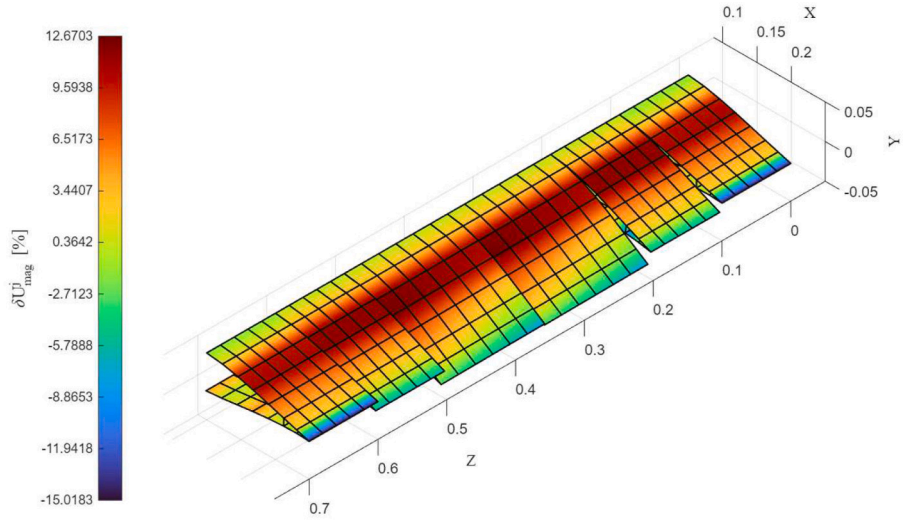

(a) 1-cosine target shape.

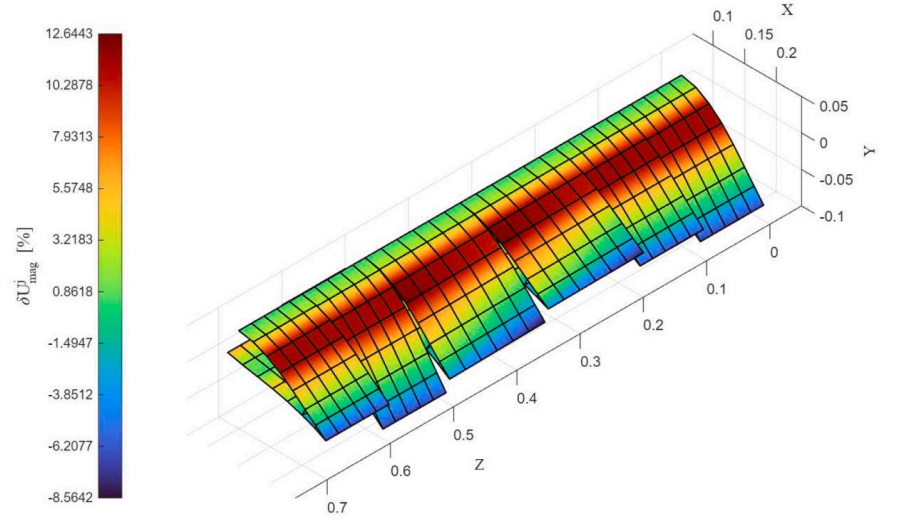

(b) Large-deflection target shape.

Fig. 17. Original control scheme, $V = 0$ m/s: final iFEM reconstructed shapes; δU^j_{mag} color-map; noise-free.

sent a realistic flight condition. This value is deliberately adopted as a numerical stress test, since it generates a sufficiently severe aerodynamic disturbance to highlight the oscillatory behavior of the original control scheme and to assess the robustness of the LM update. As shown in Fig. 15, in fact, while the original control scheme (Fig. 15a) exhibits significant oscillations during the iterative process, converging toward the target shape only after many iterations, the proposed LM method (Fig. 15b) maintains high stability. By adaptively tuning the damping parameter, the LM algorithm suppresses these oscillations and converges to the target solution in only a few iterations, maintaining a final error value of around 1% for the upper skin and 5% for the lower skin.

The physical origin of this improvement can be related to the interaction between the fixed influence-coefficients matrix and the aerodynamic response updated during the closed-loop iterations. The matrix **C** is computed once and remains unchanged throughout the control process, whereas the aerodynamic pressure is recalculated at every iteration from the current deformed airfoil profile. Consequently, especially at high airspeeds, the effective relation between an actuation-load increment and the resulting wing shape depends on the current aerodynamic state and may not be fully represented by the fixed linear mapping provided by **C**. The original controller applies the complete least-squares correction predicted by this mapping, which can therefore become excessively aggressive and produce successive overcorrections. In the LM scheme, an unsuccessful correction causes λ to increase, attenuating the subsequent load increment and interrupting the oscillatory sequence. Once the cost function decreases, λ is progressively reduced, allowing the update to recover the faster least-squares behavior.

4.2. Modular morphing wing

As anticipated in Section 2.2, and consistently with the results discussed for the composite morphing trailing edge, the numerical assessment of the modular wing is carried out by considering different intensities of the aerodynamic pressure distribution. For each module, the pressure field is evaluated with respect to a reference airfoil section and is then assumed to be constant along the module span. Its intensity is

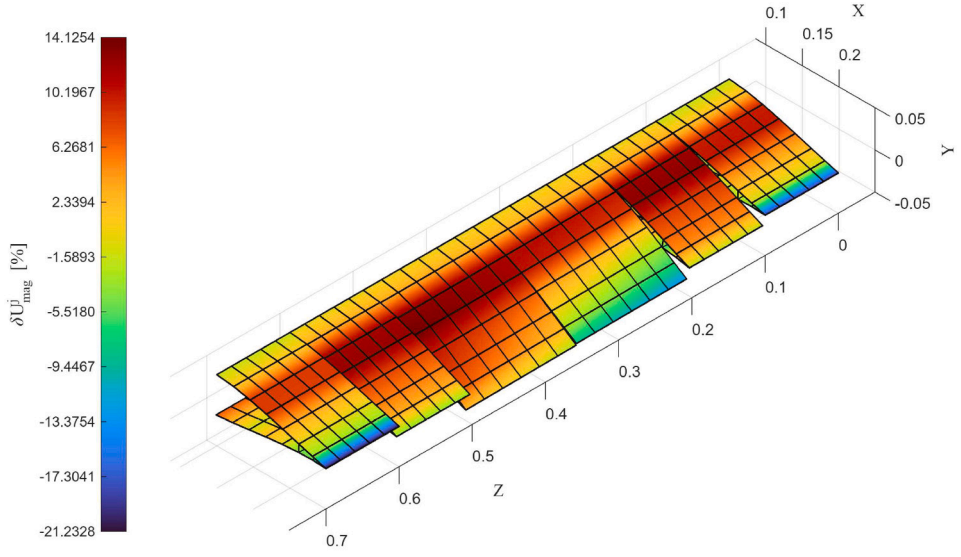

(a) 1-cosine target shape.

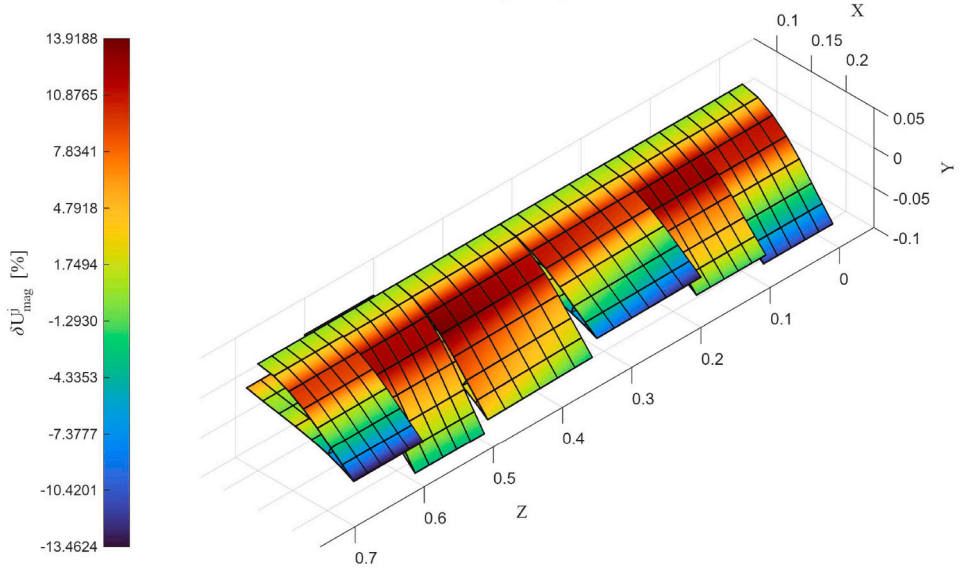

(b) Large-deflection target shape.

Fig. 18. Original control scheme, $V = 0$ m/s: final iFEM reconstructed shapes; δU^j_{mag} color-map; 10% strain noise.

regulated through the relative airspeed with respect to the external flow, in full analogy with the procedure adopted for the previous subsection (Eq. (41)).

The assessment is organized into four steps, addressing the baseline control response and its robustness to strain-measurement noise, a weighted refinement of the load-update procedure aimed at improving local shape tracking, the influence of aerodynamic disturbances, and the extension to the LM-based controller.

4.2.1. *Baseline control response and noise robustness*

The first set of results is obtained by considering the original control scheme and neglecting aerodynamic loads, i.e., by setting $V = 0$ m/s. Both the 1-cosine target shape and the large-deflection target shape introduced in Section 3.2.3 are considered. The results are presented in terms of the module-level convergence metric $err^m_d(t)$ (Fig. 16), together with the final iFEM reconstructions of the deformed structure (Fig. 17). In the latter plots, the reconstructed shape at the last control iteration is colored according to the signed nodal relative error between the target displacement magnitude, defined in Eq. (35), and the corresponding iFEM value. For the jth node, such an error is defined as

$$\delta U^j_{mag} = 100 \frac{U^j_{mag,iFEM} - U^j_{mag,tgt}}{\max\left(\mathbf{U}_{mag,tgt}\right)}. \tag{42}$$

To assess the robustness of the complete control architecture against strain-measurement uncertainty, 1000 closed-loop simulations were generated through Latin Hypercube Sampling. At each control iteration, an independent zero-mean Gaussian perturbation was applied to every strain measurement, with a standard deviation equal to 10% of the corresponding absolute nominal strain value. Fig. 16 reports the noise-free, the median err^m_d histories obtained from the noisy simulations, and the corresponding pointwise 1st–99th percentile intervals. The noise-free histories of err^m_d reported in Fig. 16 show that, for both target configurations, the original controller is able to drive all modules toward the desired shape. At the final control iteration, the maximum error among the upper and lower surfaces of all modules is approximately 0.73 mm for the 1-cosine case, against a maximum target displacement of 7.53 mm (Fig. 12), and 1.76 mm for the large-deflection case, against a maximum target displacement of 19.24 mm (Fig. 13). These results are corroborated by the noise-free colored reconstructions in Figs. 17a and 17b,

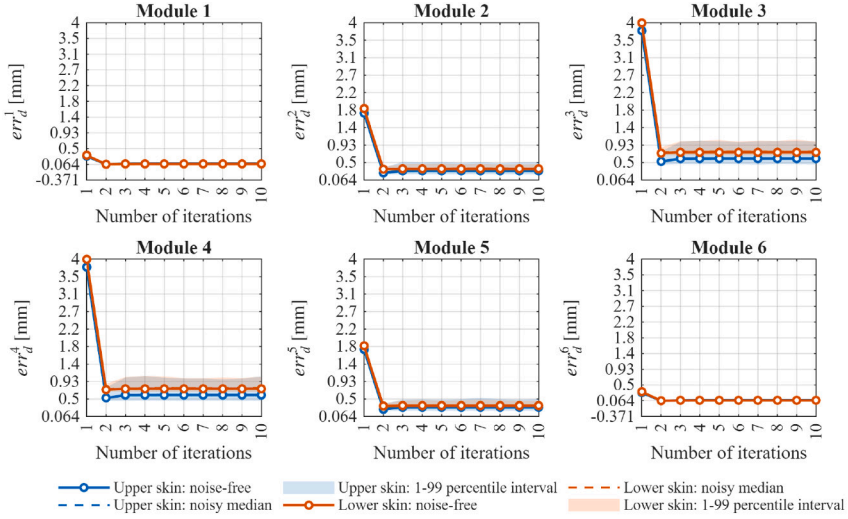

(a) 1-cosine target shape.

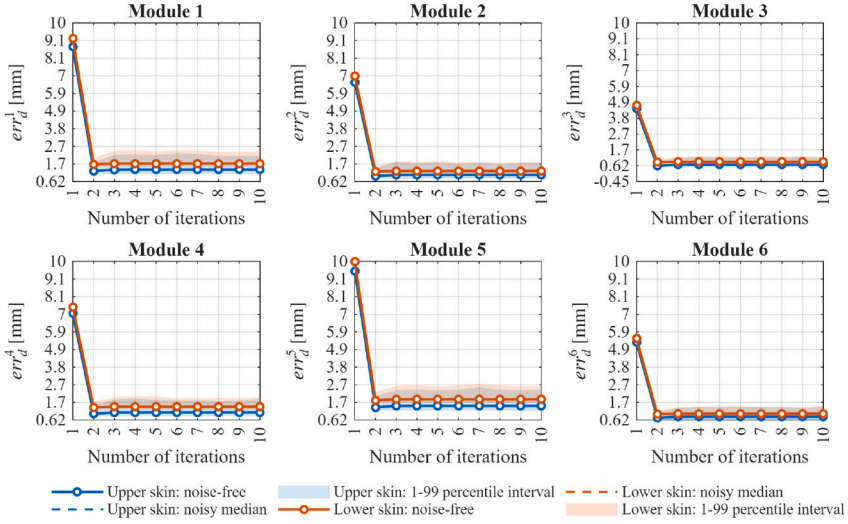

(b) Large-deflection target shape.

Fig. 19. Original control scheme with weighting matrix, $V = 0$ m/s: noise-free and noisy histories of $err_d^m(t)$.

which show signed nodal relative errors ranging approximately from +12.6% to −15.0% for the 1-cosine target and from +12.6% to −8.5% for the large-deflection target.

The Monte Carlo results show that measurement noise produces only a limited modification of the convergence behavior. The noisy median error trends remain close to the corresponding noise-free responses, while the uncertainty bands do not indicate any loss of closed-loop stability. At the final iteration, the maximum 99th-percentile error remains below approximately 0.93 mm for the 1-cosine target and 2.4 mm for the large-deflection target. The representative noisy reconstructions shown in Figs. 18a and 18b exhibit error ranges of approximately +14.12% to −21.54% and +13.91% to −13.46%, respectively. Therefore, although the strain perturbations increase the dispersion of the reconstruction and the local nodal discrepancies, they do not substantially alter the convergence of the control procedure or its capability to reproduce either target configuration. As the closed-loop response remains robust even under a substantial strain-noise level, the subsequent analyses are discussed by adopting the conservative 10% noise condition, while the corresponding noise-free trends are retained in the convergence plots as references.

4.2.2. *Weighted load-update strategy*

When the color-maps are compared with the target-displacement fields of Figs. 12 and 13, it emerges that, in both noise-free and noisy conditions, the highest positive errors are mainly located in regions where the prescribed displacement is small and therefore correspond to limited absolute discrepancies. Conversely, the largest negative errors localize at the trailing-edge tip, where the target displacement reaches its maximum. This indicates that the most critical mismatch produced by the control scheme is associated with an underestimation of the target deformation in the most demanding portion of the morphing region.

To specifically improve the shape-matching capability in this critical region, the weighted least-squares strategy proposed by Roy et al. [61] is introduced. In particular, the functional used to compute the load increments from the influence-coefficients matrix is modified as

$$\min_{\Delta\mathbf{L}(t)} \left\| \mathbf{W}^{1/2} \left(\mathbf{D}_{req}(t) - \mathbf{C}\Delta\mathbf{L}(t) \right) \right\|^2, \tag{43}$$

introducing $\mathbf{W}$, the diagonal matrix of weighting coefficients. This matrix is built so as to assign a specific weight value to each node of the iFEM mesh: 1 for the nodes where a strong correlation between the target and reconstructed shape is desired, and 10^{-2} where a weaker enforcement is allowed. Thus, in the present application, the coefficients associated with the trailing-edge nodes are set to 1, while the remaining coefficients are assigned the value 10^{-2}. The solution of the weighted least-squares problem yields

$$\Delta\mathbf{L}(t) = \left(\mathbf{C}^T\mathbf{W}\mathbf{C} \right)^{-1} \mathbf{C}^T\mathbf{W}\,\mathbf{D}_{req}(t). \tag{44}$$

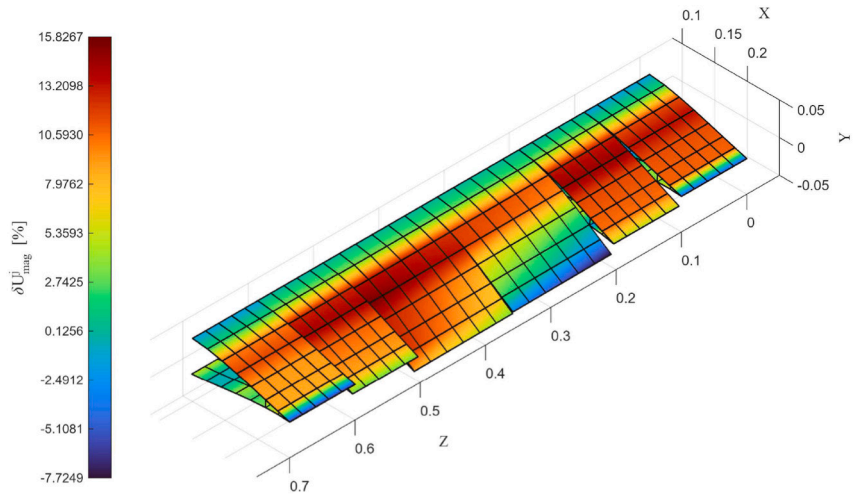

(a) 1-cosine target shape.

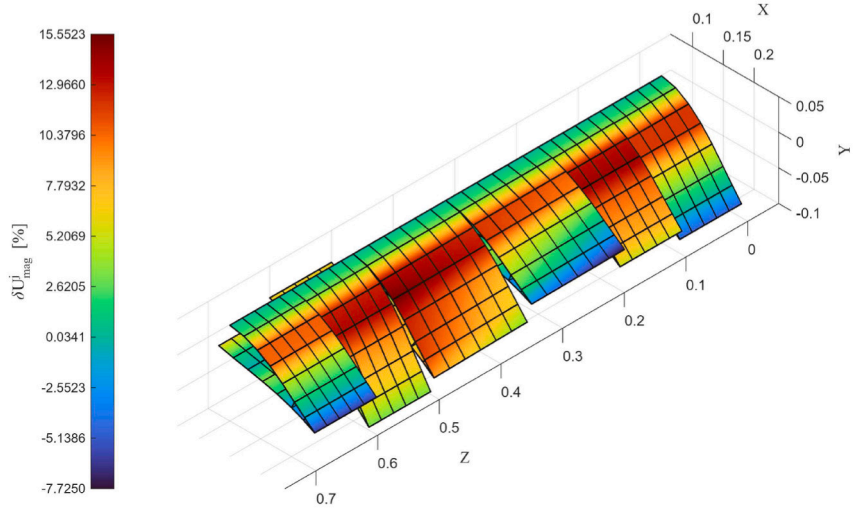

(b) Large-deflection target shape.

Fig. 20. Original control scheme with weighting matrix, $V = 0$ m/s: final iFEM reconstructed shapes with δU^j_{mag} color-map; 10% strain noise.

By adopting Eq. (44), the two cases are re-analyzed under the same 10% strain-noise condition. The corresponding trends of err^m_d, shown in Fig. 19, remain close to those obtained without weighting. At the final control iteration, the maximum 99th-percentile errors are approximately 1.06 mm for the 1-cosine target and 2.68 mm for the large-deflection target, whereas the corresponding noise-free values are approximately 0.75 mm and 1.87 mm. Thus, the weighting coefficients produce only a modest increase in the global convergence metric while redistributing the control accuracy toward the most relevant trailing-edge region.

While the positive side of the signed relative error remains of the same order as in the unweighted noisy cases, a marked reduction is observed for the negative values in the trailing-edge tip region. More specifically, the error ranges become approximately +15.72% to −7.73% for the 1-cosine target and +15.55% to −7.73% for the large-deflection target. By comparison, the corresponding unweighted noisy ranges were +14.12% to −21.54% and +13.91% to −13.46%, respectively. Therefore, the introduction of the weighting coefficients leaves the highest positive errors almost unchanged, but substantially improves the control of the tip region by reducing the negative errors where the required displacement is maximum. As in the previous case, the largest positive values remain associated with regions of relatively small prescribed displacement and therefore correspond to limited absolute discrepancies. Conversely, the reduction of the tip error results in a significant improvement in convergence toward the target deflection.

This interpretation is corroborated by the corresponding FEM deformed shapes at the last control iteration, reported in Fig. 21 and colored with the FEM nodal displacement magnitude in the XY plane, $U^j_{mag,FEM}$.

When these results are compared with the target configurations of Figs. 12 and 13, it is evident that the final deformed shapes remain close to the prescribed ones even when the feedback strains are affected by substantial noise. This confirms that the weighting strategy effectively increases the control authority over the critical tip region while preserving the overall convergence properties and noise robustness of the original scheme. Here, it is worth recalling that the FE model simulates the real morphing structure. Accordingly, the FE results of Fig. 21 are considered unknown during the closed-loop iterations, since the structural shape is reconstructed only through the iFEM. The FE results are reported here solely to demonstrate that the accuracy of the iFEM-based reconstruction is sufficient to control the morphing shape without directly measuring it.

4.2.3. Influence of aerodynamic disturbances

To account for the presence of an external disturbance, two additional airspeed levels are considered, namely $V = 50$ m/s and $V = 100$

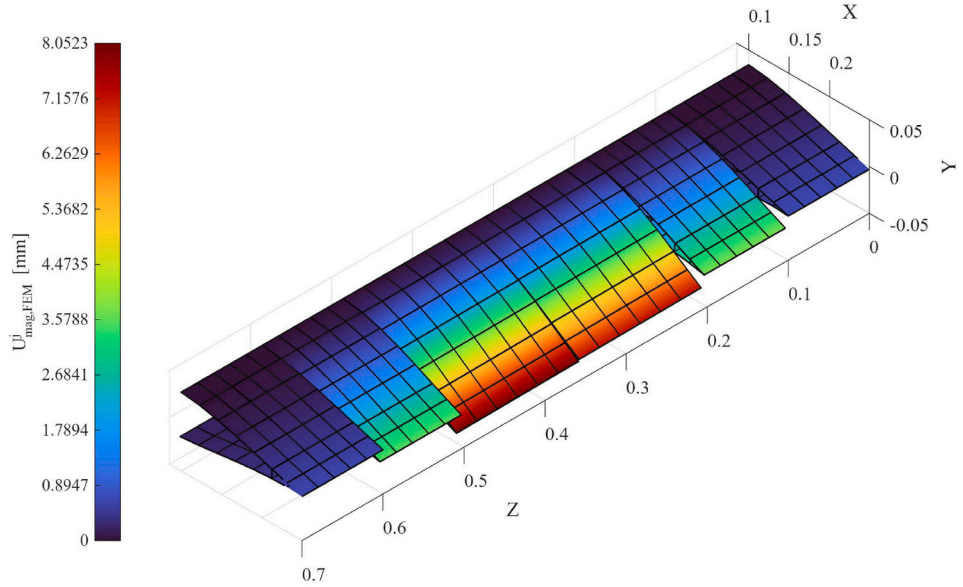

(a) 1-cosine target shape.

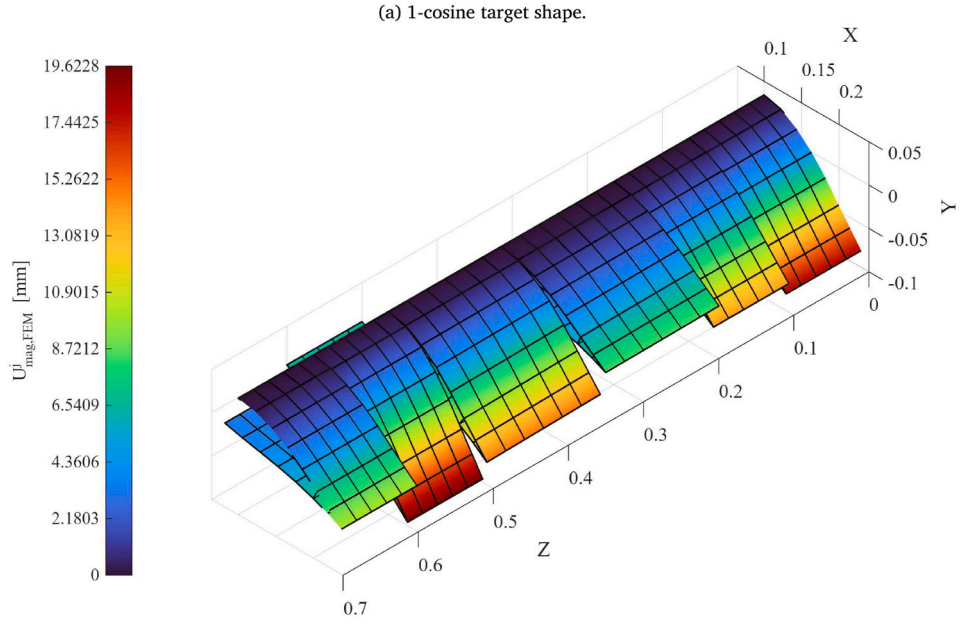

(b) Large-deflection target shape.

Fig. 21. Original control scheme with weighting matrix, $V = 0$ m/s: final FEM deformed shapes with $U^j_{mag,FEM}$ color-map; 10% strain noise.

m/s. The former is selected because it corresponds to the operating speed envisaged for the tests planned within WP4 of the MechaTwing project, whereas the latter is considered as an extreme operating condition. The weighted formulation of Eq. (44) and the conservative 10% strain-noise level are adopted for both cases. For brevity, only the results associated with the 1-cosine target shape are reported, as analogous considerations can be drawn for the large-deflection case.

The results obtained for both $V = 50$ m/s and $V = 100$ m/s, reported in Figs. 22 and 23, show that the control procedure still reaches the prescribed configuration. The maximum final 99th-percentile values of err_d^m remain close to 1.05 mm for both airspeeds and are therefore practically identical to those obtained in the corresponding undisturbed noisy case.

Likewise, the increase in aerodynamic disturbance does not produce appreciable variations in the signed nodal relative error shown by the corresponding final iFEM reconstructions.

The signed relative-error ranges are approximately +15.56% to −7.70% for $V = 50$ m/s and +15.82% to −7.90% for $V = 100$ m/s, which closely match the values obtained for the weighted undisturbed case. A plausible explanation is that the modular structure considered here is significantly stiffer than the composite morphing trailing edge analyzed in the previous subsection. As a consequence, the aerodynamic forces associated with the selected airspeeds have a much smaller influence on the structural response than the actuation loads required to morph the wing. The same conclusion therefore remains valid when substantial uncertainty affects the strain feedback.

4.2.4. *Extension to the LM-based controller*

Since no significant oscillatory behavior is observed in the modular-wing case, the original controller already proves sufficient to drive the structure toward the target configuration. Nevertheless, the Levenberg-Marquardt scheme is also tested in order to verify that the updated control framework can be naturally extended to the present configuration and to the weighted formulation introduced above. By defining

$$\mathbf{A} = \mathbf{C}^T\mathbf{W}\mathbf{C}, \qquad \mathbf{\Gamma} = diag(\mathbf{A}), \tag{45}$$

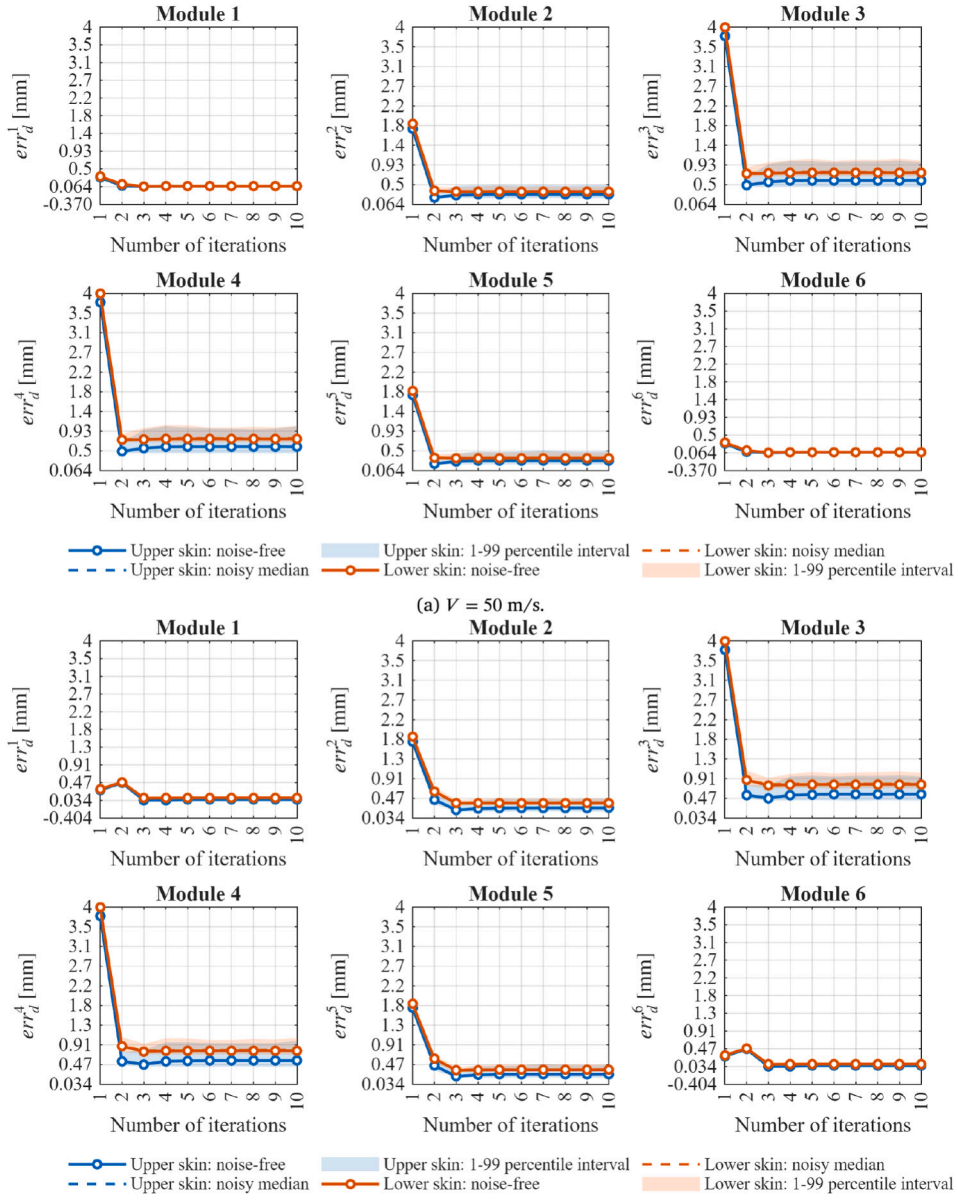

(a) $V = 50$ m/s.

(b) $V = 100$ m/s.

Fig. 22. Original control scheme with matrix of weighting coefficients, 1-cosine target shape: noise-free and noisy histories of $err_d^m(t)$.

the LM update assumes the form

$$\Delta \mathbf{L}(t) = (\mathbf{A} + \lambda \mathbf{\Gamma})^{-1} \mathbf{C}^T \mathbf{W}\, \mathbf{D}_{req}(t), \tag{46}$$

which is here applied to the $V = 100$ m/s, 1-cosine case, selecting the same LM parameters of the composite trailing edge application, that is $\lambda_0 = 1 \times 10^{-3}$, $\lambda_{df} = 1.2$, and $\lambda_{uf} = 10$, respectively.

The corresponding results, shown in Fig. 24, indicate that the LM-based scheme does not introduce appreciable modifications either in the trend of err_d^m or in the final values of the signed nodal relative error.The maximum final 99th-percentile value of err_d^m is approximately 1.02 mm, compared with a noise-free value of approximately 0.78 mm.

The representative noisy reconstruction exhibits a signed nodal relative-error range of approximately +13.96% to −7.10%, which is fully consistent with the results obtained using the original weighted controller. This confirms that the proposed update strategy can be seamlessly adapted to the modular-wing configuration, to the weighted least-squares formulation, and to uncertain strain feedback, without altering the convergence characteristics when the external disturbance is not strong enough to trigger oscillatory behavior. At the same time, the LM framework preserves the additional robustness that becomes beneficial in the presence of more severe disturbances, as already shown for the composite morphing trailing-edge benchmark.

4.3. Computational cost assessment

The real-time capability of iFEM-based shape sensing has been extensively discussed in the literature [37] and, for SSB-iFEM, experimentally demonstrated under dynamic wind-tunnel conditions [39]. To complement these previous findings and assess the computational requirements of the proposed control architecture, the execution times of the different operations were measured for the final modular-wing case, involving the weighted LM controller, the 1-cosine target shape, and an airspeed of $V = 100$ m/s.

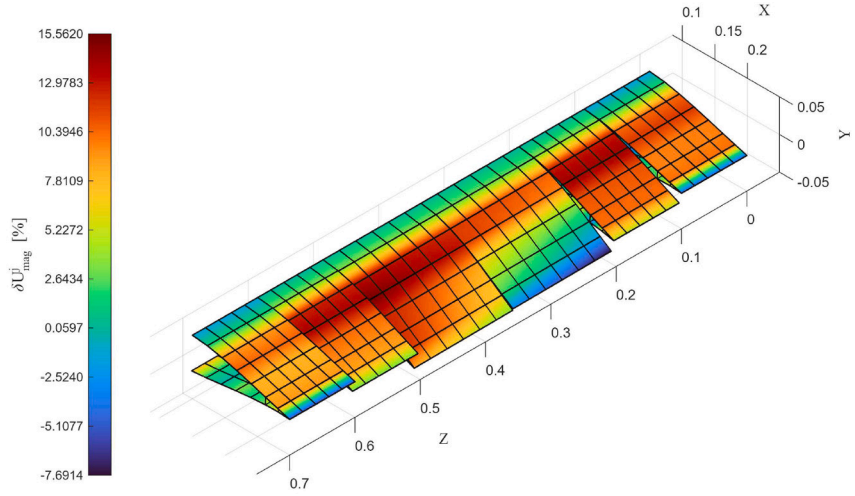

(a) $V = 50$ m/s.

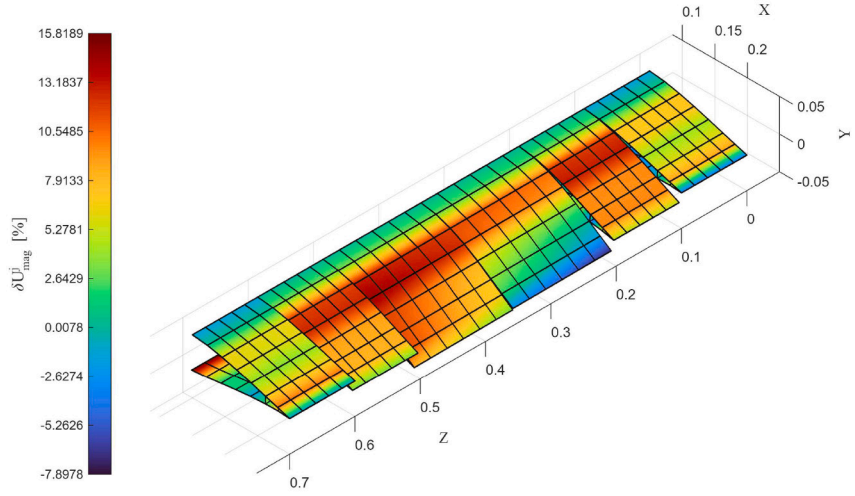

(b) $V = 100$ m/s.

Fig. 23. Original control scheme with matrix of weighting coefficients, 1-cosine target shape: final iFEM reconstructed shapes with δU^j_{mag} color-map; 10% strain noise.

As highlighted by the dashed orange box in Fig. 4, the aerodynamic-load evaluation and the direct FE analysis constitute the numerical simulation of the real morphing-wing actuation and deformation. These operations replace the physical response of the wing in the present numerical framework and would therefore not be performed by the controller in an actual implementation. Their execution times are reported separately for completeness and are not included in the computational cost of the online monitoring and control procedure. Conversely, the inverse FE analysis, the LM Update Subsystem, and the evaluation of the convergence criterion represent operations that would be performed online.

The analyses were performed on an ASUS TUF Dash F15 FX517ZC laptop equipped with a 10-core Intel Core i7-12650H processor (2.30 GHz), 16 GB of RAM, and a 64-bit Windows 11 Home operating system. The control procedure was executed serially using MATLAB R2025a. The values reported in Table 2 correspond to the average execution times measured over the control iterations.

As expected, the largest computational contribution is associated with the numerical evaluation of the aerodynamic loads. However, this operation, together with the structural FE response, belongs to the numerical simulation of the physical wing and does not represent an online control cost. The actual closed-loop monitoring and control operations require an average total time of 19.90 ms. In particular, the SSB-iFEM reconstruction and the complete LM Update Subsystem require only 0.32 ms and 0.18 ms, respectively, corresponding to a combined execution time of approximately 0.50 ms. These results confirm the low computational burden of the two core algorithmic components and indicate that the proposed framework is compatible with real-time control implementation.

Table 2
Average computational times of the operations involved in the LM-based modular-wing control analysis.

Operation	Mean computational time [ms]
Numerical simulation of the real morphing-wing actuation and deformation	
Structural FE response	1.68
Aerodynamic loads	143.95
Subtotal	**145.63**
Closed-loop monitoring and control operations	
Inverse FE Model	0.32
LM Update Subsystem	0.18
Error evaluation and convergence check	19.39
Subtotal	**19.90**

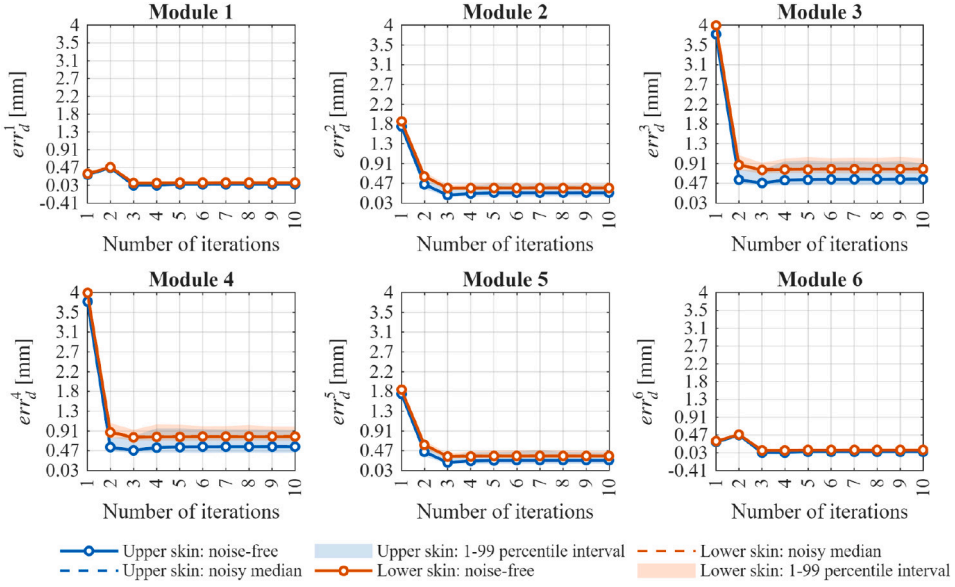

(a) Noise-free and noisy histories of $err_d^m(t)$.

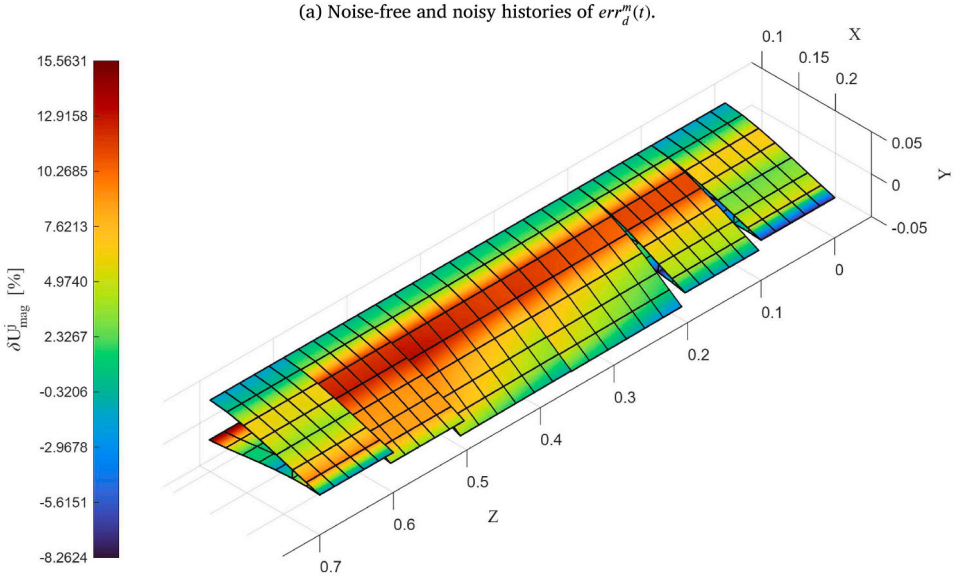

(b) Final iFEM reconstructed shape; δU_{mag}^j color-map.

Fig. 24. LM control scheme with matrix of weighting coefficients, $V = 100$ m/s, 1-cosine target shape; 10% strain-noise.

5. Conclusions

In morphing-wing applications, the possibility of achieving and maintaining a prescribed aerodynamic shape depends not only on the actuation system, but also on the capability to monitor the actual deformed configuration of the structure during operation. In this context, the inverse Finite Element Method (iFEM) plays a central role, since it enables the reconstruction of the global deformed shape from strain measurements, without requiring prior knowledge of the applied loads or material properties.

On this basis, Biscotti et al. proposed an iFEM-based closed-loop architecture for morphing-wing shape control, in which shape sensing is directly integrated into the control-loop [25]. The present work updates that control framework by introducing a new load computation strategy based on the Levenberg-Marquardt method (LM), and assesses its performance on two different benchmarks, namely the composite morphing trailing edge previously introduced in [25] and a new modular morphing wing configuration representative of the WP4 activities within the MechaTwing project.

The study showed that the proposed LM method improves the robustness of the original control strategy under severe aerodynamic loading, mitigating the oscillatory behavior observed in the composite morphing trailing edge while preserving accurate convergence to the prescribed target shape.

For the modular wing, the results also demonstrated the compatibility of the control architecture with the newly developed SSB-iFEM formulation, which enabled a hybrid back-to-back and single-sided optimized strain sensor configuration on the structure. Additionally, a weighted least-squares load-update scheme was tested, which enabled accurate reconstruction and control of the target configurations.

The uncertainty-propagation analyses further showed that the SSB-iFEM reconstruction and the complete closed-loop response remain robust under substantial strain-measurement noise, without evidence of numerical instability or loss of convergence.

Due to its higher stiffness, the modular architecture showed limited sensitivity to the aerodynamic disturbance levels considered in this work, making the original weighted controller already effective in those scenarios. Nonetheless, the LM-based extension was shown to adapt consistently to the new configuration without degrading the convergence behavior. The computational-cost assessment also confirmed the low burden of the core SSB-iFEM reconstruction and LM update operations, supporting the applicability of the proposed architecture to online shape monitoring and control.

Overall, the numerical results confirm the potential of iFEM/SSB-iFEM-based feedback strategies as efficient and versatile tools for shape control of morphing wing structures, supporting their application to increasingly realistic aerospace systems.

Future work will focus on the experimental validation of the complete closed-loop architecture on a physical, instrumented morphing-wing structure.

CRediT authorship contribution statement

Vincenzo Biscotti: Writing – review & editing, Writing – original draft, Visualization, Validation, Software, Methodology, Investigation, Formal analysis, Data curation, Conceptualization; **David Blaha:** Writing – review & editing, Writing – original draft, Visualization, Validation, Software, Methodology, Investigation, Formal analysis, Data curation; **Milan Růžička:** Writing – review & editing, Supervision; **Marco Gherlone:** Writing – review & editing, Supervision, Methodology, Conceptualization.

Declaration of competing interest

The authors declare the following financial interests/personal relationships which may be considered as potential competing interests: Vincenzo Biscotti reports financial support was provided by Italian Ministry of University and Research (MUR) and the Sustainable Mobility Center (MOST). Marco Gherlone reports financial support was provided by Italian Ministry of University and Research (MUR) and the Sustainable Mobility Center (MOST). If there are other authors, they declare that they have no known competing financial interests or personal relationships that could have appeared to influence the work reported in this paper.

Acknowledgements

This work was possible thanks to the grant released within the Framework Programme for Research and Innovation (2021–2027), grant n∘ 101159722, with project name “TWINNING FOR EXCELLENCE IN MORPHING AND AEROMECHATRONIC WING CONTROL: A LEAP TOWARDS ECO-SMART AVIATION” acronym(MechaTwing).

Vincenzo Biscotti and Marco Gherlone acknowledge the support of the Italian Ministry of University and Research (MUR) and the Sustainable Mobility Center (MOST) through the project PNRR - M4C2 - CNMS - Spoke 1, funded under the scheme CN00000023 - PNRR–M4C2 Inv. 1.4 with grant agreement num. 55_PRR22_1155_22_GG002138.

Data availability

Data will be made available on request.

References

[1] S. Barbarino, O. Bilgen, R.M. Ajaj, M.I. Friswell, D.J. Inman, A review of morphing aircraft, J. Intell. Mater. Syst. Struct. 22 (9) (2011) 823–877. https://doi.org/10.1177/1045389X11414084

[2] M.N. Mowla, D. Asadi, T. Durhasan, J.R. Jafari, M. Amoozgar, Recent advancements in morphing applications: architecture, artificial intelligence integration, challenges, and future trends-a comprehensive survey, Aerosp. Sci. Technol. 161 (2025) 110102. https://doi.org/10.1016/j.ast.2025.110102

[3] D. Li, S. Zhao, A. Da Ronch, J. Xiang, J. Drofelnik, Y. Li, L. Zhang, Y. Wu, M. Kintscher, H.P. Monner, A. Rudenko, S. Guo, W. Yin, J. Kirn, S. Storm, R.D. 2Breuker, A review of modelling and analysis of morphing wings, Prog. Aerosp. Sci. 100 (2018) 46–62. https://doi.org/10.1016/j.paerosci.2018.06.002

[4] S. Ameduri, A. Concilio, Morphing wings review: aims, challenges, and current open issues of a technology, Proc. Inst. Mech. Eng. C: J. Mech. Eng. Sci. 237 (18) (2023) 4112–4130. https://doi.org/10.1177/0954406220944423

[5] A. Pankonien, Smart Material Wing Morphing for Unmanned Aerial Vehicles, 2015, https://www.researchgate.net/publication/295417494

[6] G. Servetti, E. Cestino, G. Frulla, Numerical investigation of different morph wing configurations for the rolling maneuver, J. Intell. Mater. Syst. Struct. 1045389X261422196. https://doi.org/10.1177/1045389X261422196

[7] G. Servetti, E. Cestino, G. Frulla, Parametric evaluation of morphed wing effectiveness, Aerospace 13 (2) (2026). https://doi.org/10.3390/aerospace13020187

[8] J.N. Kudva, B.P. Sanders, J.L. Pinkerton-Florance, E. Garcia, Overview of the DARPA/AFRL/NASA smart wing phase II program, in: A.-M.R. McGowan (Ed.), Smart Structures and Materials 2001: Industrial and Commercial Applications of Smart Structures Technologies, 4332, International Society for Optics and Photonics, SPIE, 2001, pp. 383 – 389. https://doi.org/10.1117/12.429678

[9] I. Dimino, G. Diodati, A. Concilio, A. Volovick, L. Zivan, Distributed electromechanical actuation system design for a morphing trailing edge wing, in: S.F. Griffin (Ed.), Industrial and Commercial Applications of Smart Structures Technologies 2016, 9801, International Society for Optics and Photonics, SPIE, 2016, p. 980108. https://doi.org/10.1117/12.2219223

[10] M. Arena, F. Amoroso, R. Pecora, S. Ameduri, Electro-actuation system strategy for a morphing flap, Aerospace 6 (1) (2019). https://doi.org/10.3390/aerospace6010001

[11] Twinning for Excellence in Morphing and Aero-Mechatronic Wing Control: A Leap Towards Eco-Smart Aviation, 2024, https://doi.org/10.3030/101159722

[12] M.C. Noviello, B. Galasso, I. Dimino, S. Ameduri, A. Concilio, Trade-off conceptual design of a camber morphing flap for the next generation hybrid electrical aircraft across the HERWINGT project, Appl. Sci. 15 (7) (2025). https://doi.org/10.3390/app15073660

[13] J.A. Hetrick, R.F. Osborn, S. Kota, P.M. Flick, D.B. Paul, Flight testing of mission adaptive compliant wing, Collect. Tech. Pap. - AIAA/ASME/ASCE/AHS/ASC Struct. Struct. Dyn. Mater. Conf. 1 (2007) 92–109. https://doi.org/10.2514/6.2007-1709

[14] T. Lin, R. Pecora, D. Ciliberti, W. Xia, S. Hu, Aerodynamic optimization of an adaptive flap for next-generation green aircraft, Chin. J. Aeronaut. 37 (2) (2024) 100–122. https://doi.org/10.1016/j.cja.2023.10.010

[15] S. Ameduri, B. Galasso, M.C. Noviello, I. Dimino, A. Concilio, P. Catalano, F.A. D’Aniello, G.M. Carossa, L. Pinazo, J. Derry, B. Biju, S. Shreedharan, Design and optimization of a compliant morphing trailing edge for high-lift generation, Appl. Sci. 15 (5) (2025). https://doi.org/10.3390/app15052529

[16] V. Alulema, V. Hidalgo, E. Cando, E. Valencia, Design optimization of a pseudo-rigid-compliant mechanism for large, continuous, and smooth morphing of airfoil camber, Aerospace 12 (9) (2025). https://doi.org/10.3390/aerospace12090825

[17] J.R. Rivas-Padilla, D.M. Boston, K. Boddapati, A.F. Arrieta, Aero-structural optimization and actuation analysis of a morphing wing section with embedded selectively stiff bistable elements, J. Compos. Mater. 57 (4) (2023) 737–757. https://doi.org/10.1177/00219983231155163

[18] C. Wang, Z. Wang, H. Wang, Z. Chen, Y. Tian, Y. Yang, S. Yin, Customized deformation behavior of morphing wing through reversibly assembled multi-stable metamaterials, Smart Mater. Struct. 33 (4) (2024) 045015. https://doi.org/10.1088/1361-665X/ad2e3a

[19] A. Dharmdas, A.Y. Patil, A. Baig, O.Z. Hosmani, S.N. Mathad, M.B. Patil, R. Kumar, B.B. Kottureshettar, I.M.R. Fattah, An experimental and simulation study of the active camber morphing concept on airfoils using bio-inspired structures, Biomimetics 8 (2) (2023). https://doi.org/10.3390/biomimetics8020251

[20] M.H. Negahban, A. Hallonet, M. Noupoussi Woumeni, C. Nguyen, R.M. Botez, Structural and topological optimization of a novel elephant trunk mechanism for morphing wing applications, Aerospace 12 (5) (2025). https://doi.org/10.3390/aerospace12050381

[21] A. Pankonien, D.J. Inman, Experimental testing of spanwise morphing trailing edge concept, in: H. Sodano (Ed.), Active and Passive Smart Structures and Integrated Systems 2013, 8688, International Society for Optics and Photonics, SPIE, 2013, p. 868815. https://doi.org/10.1117/12.2009400

[22] A.M. Pankonien, D.J. Inman, Aerodynamic performance of a spanwise morphing trailing edge concept, in: Proceedings of the 25th International Conference on Adaptive Structures and Technologies (ICAST 2014), The Hague, The Netherlands, 2014, pp. 1–12.

[23] L. CHU, Q. LI, F. GU, X. DU, Y. HE, Y. DENG, Design, modeling, and control of morphing aircraft: a review, Chin. J. Aeronaut. 35 (5) (2022) 220–246. https://doi.org/10.1016/j.cja.2021.09.013

[24] M.S. Parancheerivilakkathil, J.S. Pilakkadan, R.M. Ajaj, M. Amoozgar, D. Asadi, Y. Zweiri, M.I. Friswell, A review of control strategies used for morphing aircraft applications, Chin. J. Aeronaut. 37 (4) (2024) 436–463. https://doi.org/10.1016/j.cja.2023.12.035

[25] V. Biscotti, R. Roy, M. Gherlone, Shape monitoring of morphing wing structures using the inverse finite element method, Comput. Struct. 309 (2025) 107652. https://doi.org/10.1016/j.compstruc.2025.107652

[26] A. Tessler, J. Spangler, A least-squares variational method for full-field reconstruction of elastic deformations in shear-deformable plates and shells, Comput. Methods Appl. Mech. Eng. 194 (2) (2005) 327–339. Selected papers from the 11th Conference on The Mathematics of Finite Elements and Applications. https://doi.org/10.1016/j.cma.2004.03.015

[27] M. Gherlone, P. Cerracchio, M. Mattone, Shape sensing methods: review and experimental comparison on a wing-shaped plate, Prog. Aerosp. Sci. 99 (April, 2018) 14–26. https://doi.org/10.1016/j.paerosci.2018.04.001
[28] M. Esposito, M. Gherlone, Composite wing box deformed-shape reconstruction based on measured strains: optimization and comparison of existing approaches, Aerosp. Sci. Technol. 99 (2020) 105758. https://doi.org/10.1016/j.ast.2020.105758
[29] M. Esposito, M. Gherlone, Material and strain sensing uncertainties quantification for the shape sensing of a composite wing box, Mech. Syst. Signal Process. 160 (2021) 107875. https://doi.org/10.1016/j.ymssp.2021.107875
[30] Y. Li, Z. Sharif-Khodaei, Shape sensing of composite shell using distributed fibre optic sensing, Int. J. Mech. Sci. 286 (2025) 109859. https://doi.org/10.1016/j.ijmecsci.2024.109859
[31] M. Esposito, A novel shape sensing approach based on the coupling of modal virtual sensor expansion and iFEM: numerical and experimental assessment on composite stiffened structures, Comput. Struct. 305 (2024) 107520. https://doi.org/10.1016/j.compstruc.2024.107520
[32] M. Esposito, Strain pre-extrapolation methods for shape sensing: a comparative study between modal virtual sensor expansion and smoothing element analysis, Results Eng. 29 (2026) 109109. https://doi.org/10.1016/j.rineng.2026.109109
[33] T. Huang, S. Yuan, J. Chen, T. Dong, W. Duan, Thermal deformation monitoring of large-scale composite honeycomb spaceborne antennas with limited strain measurements, Aerosp. Sci. Technol. 155 (2024) 109665. https://doi.org/10.1016/j.ast.2024.109665
[34] J. Wei, T. Huang, T. Dong, Z. Zhang, S. Yuan, An optimal sensor placement framework for iFEM-based shape monitoring using Fisher information matrix, Mech. Syst. Signal Process. 255 (2026) 114431. https://doi.org/10.1016/j.ymssp.2026.114431
[35] V. Biscotti, M. Esposito, M. Gherlone, A new single sensor based iFEM formulation for shape-sensing of thin-walled structures instrumented with single-sided sensor configurations: formulation, numerical assessment, and experimental validation, Mech. Syst. Signal Process. 232 (2025) 112700. https://doi.org/10.1016/j.ymssp.2025.112700
[36] V. Biscotti, M. Esposito, M. Gherlone, Optimal strain sensor layouts for shape sensing of thin-walled structures using the single sensor based inverse finite element method, Proc. Int. Congr. New Trends Mech. - ICNTM25 1 (2025) 162–173. https://iris.polito.it/handle/11583/3002825
[37] I. Khalid, Z.A. Qureshi, S. Oterkus, E. Oterkus, Progress in inverse finite element method for aerospace structural health monitoring applications, Prog. Aerosp. Sci. 157 (2025) 101132. https://doi.org/10.1016/j.paerosci.2025.101132
[38] T. Dong, S. Yuan, T. Huang, Real-time shape sensing of large-scale honeycomb antennas with a displacement-gradient-based variable-size inverse finite element method, Compos. Struct. 344 (2024) 118320. https://doi.org/10.1016/j.compstruct.2024.118320
[39] M. Esposito, M. Sorrenti, M. Gherlone, Experimental shape sensing of a wing structure using SSB-iFEM: static assessment and dynamic wind tunnel test, Measurement 265 (2026) 120354. https://doi.org/10.1016/j.measurement.2026.120354
[40] F. Ganjdoust, A. Kefal, A. Tessler, A novel delamination damage detection strategy based on inverse finite element method for structural health monitoring of composite structures, Mech. Syst. Signal Process. 192 (2023) 110202. https://doi.org/10.1016/j.ymssp.2023.110202
[41] J. Bardiani, R. Faure Ragani, A. Manes, C. Sbarufatti, A. Kefal, Real-time damage detection and localization in ship structures using iFEM and machine learning techniques, Ocean Eng. 343 (2026) 123379. https://doi.org/10.1016/j.oceaneng.2025.123379
[42] J. Bardiani, R. Faure Ragani, L. Pinello, A. Kefal, A. Manes, C. Sbarufatti, Shape sensing and damage detection of composite pressure vessels using inverse finite element method coupled with physics-based strain pre-extrapolation, Thin-Walled Struct. 218 (2026) 113935. https://doi.org/10.1016/j.tws.2025.113935
[43] G. Delo, R. Roy, K. Worden, C. Surace, On the use of the inverse finite element method to enhance knowledge sharing in population-based structural health monitoring, Comput. Struct. 307 (2025) 107635. https://doi.org/10.1016/j.compstruc.2024.107635
[44] U. Papa, S. Russo, A. Lamboglia, G.D. Core, G. Iannuzzo, Health structure monitoring for the design of an innovative UAS fixed wing through inverse finite element method (iFEM), Aerosp. Sci. Technol. 69 (2017) 439–448. https://doi.org/10.1016/j.ast.2017.07.005
[45] D. Oboe, L. Colombo, C. Sbarufatti, M. Giglio, Shape sensing of a complex aeronautical structure with inverse finite element method, Sensors 21 (4) (2021). https://doi.org/10.3390/s21041388
[46] M. Esposito, R. Roy, C. Surace, M. Gherlone, Hybrid shell-beam inverse finite element method for the shape sensing of stiffened thin-walled structures: formulation and experimental validation on a composite wing-shaped panel, Sensors 23 (13) (2023). https://doi.org/10.3390/s23135962
[47] J. Bardiani, D. Poloni, D. Oboe, M. Giglio, A. Manes, C. Sbarufatti, Advanced shape sensing of a full-scale composite UAV stabilizer under non-ideal boundary conditions using the inverse finite element method, Aerosp. Sci. Technol. 168 (2026) 111067. https://doi.org/10.1016/j.ast.2025.111067
[48] I. Khalid, Z.A. Qureshi, S. Oterkus, E. Oterkus, Structural health monitoring of aerospace thin plate and shell structures using the inverse finite element method (iFEM), Thin-Walled Struct. 209 (2025) 112923. https://doi.org/10.1016/j.tws.2025.112923
[49] A. Kefal, E. Oterkus, Displacement and stress monitoring of a Panamax containership using inverse finite element method, Ocean Eng. 119 (2016) 16–29. https://doi.org/10.1016/j.oceaneng.2016.04.025
[50] A. Kefal, E. Oterkus, Displacement and stress monitoring of a chemical tanker based on inverse finite element method, Ocean Eng. 112 (2016) 33–46. https://doi.org/10.1016/j.oceaneng.2015.11.032
[51] M. Li, A. Kefal, B.C. Cerik, E. Oterkus, Dent damage identification in stiffened cylindrical structures using inverse finite element method, Ocean Eng. 198 (2020) 106944. https://doi.org/10.1016/j.oceaneng.2020.106944
[52] J. Bardiani, C. Oppezzo, A. Manes, C. Sbarufatti, An inverse FEM for structural health monitoring of a containership: sensor network optimization for accurate displacement, strain, and internal force reconstruction, Sensors 25 (1) (2025). https://doi.org/10.3390/s25010276
[53] J. Wang, L. Ren, R. You, T. Jiang, Z. Jia, G. xin Wang, Experimental study of pipeline deformation monitoring using the inverse finite element method based on the iBeam3 element, Measurement 184 (2021) 109881. https://doi.org/10.1016/j.measurement.2021.109881
[54] P. Savino, F. Tondolo, Two-node curved inverse finite element formulations based on exact strain-displacement solution, J. Appl. Comput. Mech. 9 (1) (2023) 259–273. https://doi.org/10.22055/jacm.2022.41150.3708
[55] D. Poloni, M. Morgese, C. Wang, T. Taylor, M. Giglio, F. Ansari, C. Sbarufatti, Reference-free distributed monitoring of deflections in multi-span bridges, Eng. Struct. 323 (2025) 119277. https://doi.org/10.1016/j.engstruct.2024.119277
[56] D. Poloni, C. Wang, M. Morgese, T. Taylor, M. Giglio, F. Ansari, C. Sbarufatti, IFEM method for distributed monitoring of cable forces in cable-stayed bridges, Struct. Health Monit. 0 (0) (2025) 14759217251385449. https://doi.org/10.1177/14759217251385449
[57] T. Huang, T. Dong, S. Yuan, A piecewise inverse finite element method for shape sensing of the morphing wing fishbone, Smart Mater. Struct. 33 (4) (2024) 045030. https://doi.org/10.1088/1361-665X/ad2c70
[58] D.W. Marquardt, An algorithm for least-squares estimation of nonlinear parameters, J. Soc. Ind. Appl. Math. 11 (2) (1963) 431–441. https://doi.org/10.1137/0111030
[59] H.P. Gavin, The Levenberg-Marquardt algorithm for nonlinear least squares curve-fitting problems, Dep. Civ. Environ. Eng. Duke Univ. August 3 (1–23) (2019) 4.
[60] A. Kefal, E. Oterkus, A. Tessler, J.L. Spangler, A quadrilateral inverse-shell element with drilling degrees of freedom for shape sensing and structural health monitoring, Eng. Sci. Technol. Int. J. 19 (3) (2016) 1299–1313. https://doi.org/10.1016/j.jestch.2016.03.006
[61] R. Roy, C. Surace, M. Gherlone, An approach to morphing structure control based on real-time displacement reconstruction, J. Phys. Conf. Ser. 3253 (1) (2026) 012004. https://doi.org/10.1088/1742-6596/3253/1/012004
[62] M. Drela, XFOIL: an analysis and design system for low Reynolds number airfoils, Low Reynolds Number Aerodyn. Proc. Conf., Notre Dame, U.S.A., JUNE 5–7 (1989) 1–12. https://link.springer.com/chapter/10.1007/978-3-642-84010-4_1
[63] B. Berton, Shape memory alloys application: trailing edge shape control, Multifunct. Struct./ Integr. Sens. Antennas (2006) 13.1–13.16. http://www.rto.nato.int/abstracts.asp.
[64] D.P. Wang, J.D. Bartley-Cho, C.A. Martin, B.J. Hallam, Development of high-rate large-deflection hingeless trailing-edge control surface for the smart wing wind tunnel model, 2001, https://doi.org/10.1117/12.429682
[65] R. De Breuker, T. Mkhoyan, N. Nazeer, V. Stuber, X. Wang, I. Mkhoyan, R. Groves, S. van der Zwaag, J. Sodja, Overview of the SmartX wing technology integrator, Actuators 11 (10) (2022). https://doi.org/10.3390/act11100302
[66] F.V. Hutcheson, T.F. Brooks, W.M. Humphreys, Noise radiation from a continuous mold-line link flap configuration, 14th AIAA/CEAS Aeroacoustics Conf. (2008). https://doi.org/10.2514/6.2008-2966